Tectonophysics 855 (2023) 229814

Contents lists available at ScienceDirect

Tectonophysics

journal homepage: www.elsevier.com/locate/tecto

From the Lebombo Monocline to the Mozambique Deep Basin, using combined wide-angle and reflection seismic data

M. Moulin [a,*], A. Leprêtre [a], F. Verrier [a], P. Schnürle [a], M. Evain [a], P. de Clarens [b], J. Thompson [a,c], N. Dias [d], A. Afilhado [e], A. Loureiro [d], D. Aslanian [a]

[a] Geo-Ocean, Univ Brest, CNRS, Ifremer, UMR6538, F-29280 Plouzane, France
[b] TOTAL, R&D, avenue Larribau, 64000 Pau, France
[c] Univ. of Ghana, Department of Geology, Accra, Ghana
[d] IDL – Instituto Dom Luis, Faculdade das Ciencias da Universidade de Lisboa, 1749-016 Lisboa, Portugal
[e] ISEL – Instituto Superior de Engenharia de Lisboa, Lisboa, Portugal

ARTICLE INFO

Keywords:
Mozambique Channel
North Natal Valley
Sedimentary and crustal architecture
Coincident wide-angle and marine multi-channel profiles
Margin formation
Lower continental crust

ABSTRACT

The North Natal valley (NNV), South Mozambique margin, is a key area for the understanding of the SW Indian Ocean history since the Gondwana break-up as its crustal nature and geometry strongly impacted the reconstruction of the paleogeography before the rifting. It is also of considerable importance for the understanding of the evolution of a margin system as the NNV is situated at the transition between divergent and strike-slip segments and at the conjunction of Oxfordian-Kimmeridgian Indian Ocean and the Valanginian-Aptian Atlantic one. As one part of the PAMELA project (PAssive Margins Exploration Laboratories), the NNV and the East Limpopo margin have been investigated during the MOZ3/5 cruise (2016), through the acquisition of 7 intersecting wide-angle profiles and coincident marine multichannel (720 traces) seismic as well as potential field data. Simultaneously, land seismometers were deployed in the Mozambique coastal plain (MCP), extending six of those profiles on land for about 100 km in order to provide information on the onshore-offshore transition. Wide-angle seismic data are of major importance as they can highlight constraints on the crustal structure of the margin and the position of the continent-ocean boundary in an area where the crustal nature is poorly known and largely controversial. The MOZ3/5 data set therefore reveals new essential constraints for kinematic reconstructions. This work presents results on the crustal structure from P-waves velocity modeling along two *E*-W wide-angle profiles (MZ1 and MZ2) through the NNV, from the Lebombo Monocline to the Mozambique Basin (MB), and crossing the Mozambique Fracture Zone (MFZ).

The new geophysical data reveals an upper sedimentary sequence characterized by low velocities generally not exceeding 3 km/s, and up to 3 km thick where a major contouritic structure was observed. This feature formes together with several other contouritic structures, a N-S alignment just west of the MFZ, which produces high positive gravity anomalies, previously thought to be related to the magmatism that built the Galathea and Dana Plateaus. High velocity lenses are locally identified through the sedimentary layers and interpreted as interbedded volcanic sills. Furthermore, from the NNV to the MFZ, the underlying sequence is formed of a 3.0–3.5 km thick volcano-sedimentary sequence presenting important lateral changes in its seismic signature and characterized by a large velocity range (4.4 to 5.8 km/s), which partly reflects variations in the volcanic/sedimentary ratio laterally and with depth. At depth, an initially smoother and reduced eastward thinning of the crust occurs to the West below the continental shelf, from 34 to 31 km thick. The crustal thickness remains relatively constant of about 28–29 km along the Central Domain (CD), whereas a second and major region of thinning (26 to 12 km thick) is imaged West of the MFZ, in the southward prolongation of the Limpopo Corridor (LC). By contrast, as the eastern extremity, the crust is <10 km thick when reaching the MB. Crustal velocities reveal low velocity gradients, with atypical high velocities, increasing to 7.3 to 7.6 km/s at the base of the crust, and globally in the whole crust in the LC, just West of the MFZ. We interpreted the velocity architecture combined with the evidence of volcanism at shallower depths as indicative of an intensively intruded continental

* Corresponding author.
E-mail address: mmoulin@ifremer.fr (M. Moulin).

https://doi.org/10.1016/j.tecto.2023.229814
Received 11 October 2022; Received in revised form 21 February 2023; Accepted 8 March 2023
Available online 7 April 2023

crust in the NNV, and discuss the particular segmentation of the longest profile (MZ1) in the kinematic context of both divergent and strike-slipe segments offshore Mozambique.

Combining wide-angle and reflection seismic observations along these two profiles and the other MOZ3/5 lines, the data shows a coherent segmentation of the *E*-W crustal architecture off South Mozambique. These results along MZ1 and MZ2 profiles, combined with the previously published profiles, gives a 3D-view of the NNV, which becomes one of the most passive margins covered in the world by deep wide-angle seismic data.

1. Introduction

The aims of Pamela MOZ35 wide-angle experiment was to answer to questions that are still matter of debate: the architecture, the nature and position of the first oceanic crust, the link with the Lebombo mountains and MCP, the ages of volcanism, the geodynamic evolution and the timing.

Indeed, as already stressed in companion papers (e.g., Thompson et al., 2019; Moulin et al., 2020; Aslanian et al., 2021; Evain et al., 2021; Leprêtre et al., 2020; Li et al., 2021; Watremetz et al., 2021; Schnurle et al., 2023), the crustal nature in the area was the subject of a vigorous debate. Many authors, based on potential fields studies and kinematic models, have interpreted the crust in the NNV, either as thickened oceanic crust (e.g., Ludwig et al., 1968; Green, 1972; Klausen, 2009; Leinweber and Jokat, 2011; Mueller and Jokat, 2019; Tikku et al., 2002; Watts, 2001) either and/or thinned continental crust (Dingle and Scrutton, 1974; Lafourcade, 1984; Domingues et al., 2016; Hanyu et al., 2017) with high magmatic content based on scarce seismic data, potential field data, and/or geological correlation with the conjugate Antarctican margin. The crustal structure of these passive margins, is important in particular 1) to understand the transition between the strike-slip margin related to the (Oxfordian-Kimmeridgian) Africa-Antartica breakup (East Limpopo) (Evain et al., 2021; Watremetz et al., 2021; Roche et al., 2021) and the pull-apart divergent margin (NNV) (Leprêtre et al., 2020; Schnurle et al., 2023) which ended with the Valanginian Africa-South America breakup when the withdrawal of the Falkland-Malvinas Plateau was accommodated by dextral strike-slip movement along the Agulhas-Falkland Fracture Zone (e.g. Thompson et al., 2019; Mueller and Jokat, 2019); 2) to study the rifting evolution of the margin from the Lebombo monocline to the continent/ocean boundary along the Mozambique FZ and 3) to better constrain kinematic reconstructions of the Africa-Antarctica-South America breakup. Indeed, exact timing and mechanisms of Gondwana breakup remain still speculative, due to the lack of quality geological and geophysical data,

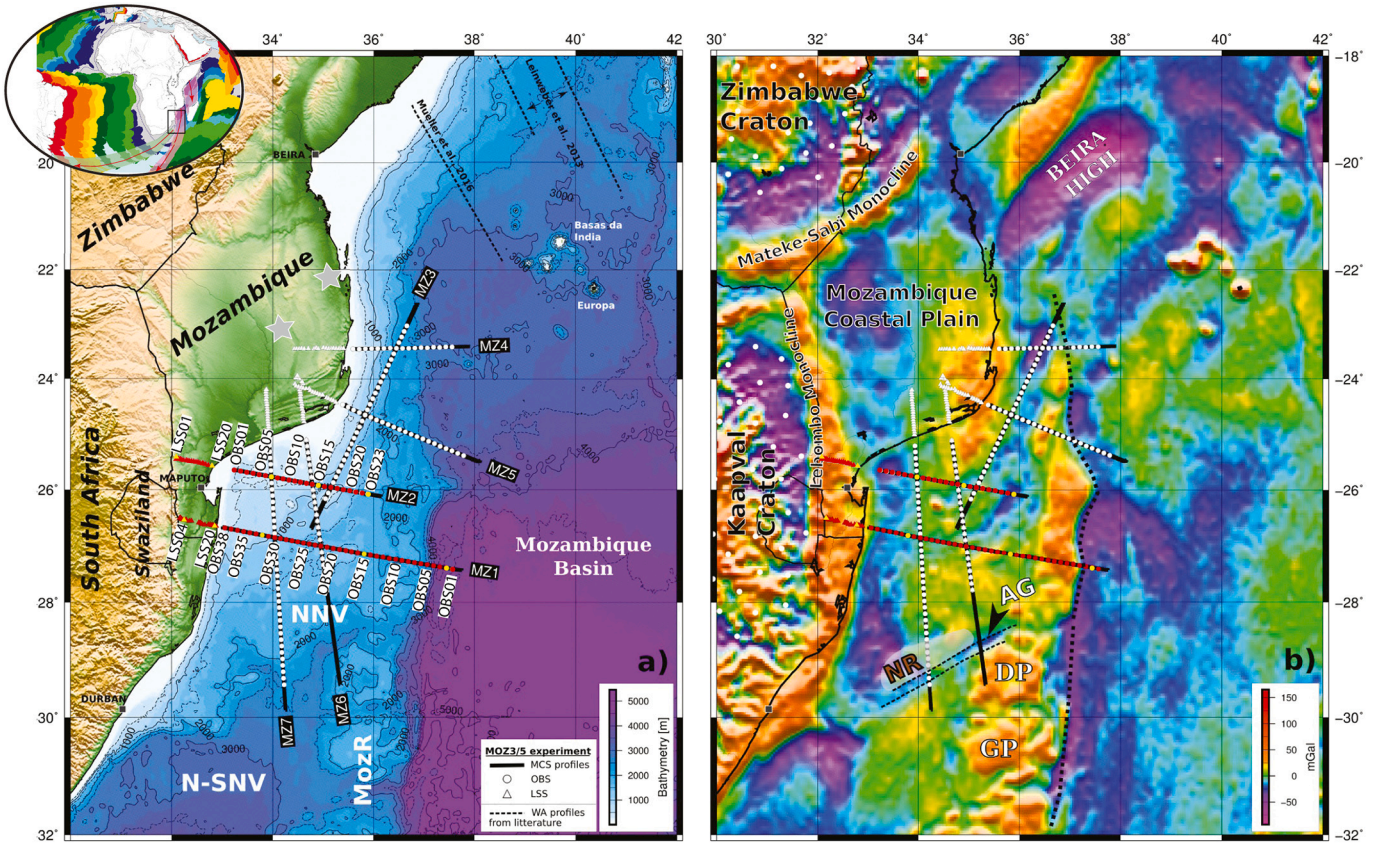

Fig. 1. : Location of the wide-angle seismic MZ1 and M2 profiles of the PAMELA MOZ3/5 experiment, South Mozambique. Inset: schematic cartoon that simplifies the geodynamic evolution of the area (a) on topographic (GMRT grid, Ryan et al., 2009) and bathymetric (GEBCO) map. The gray stars indicated the location points of 1D Vs-depth profiles from Domingues et al., 2016. (b) on free-air gravity anomaly (Sandwell and Smith, 2009). The main features known in the area are from Mueller and Jokat (2019), which are based on Leinweber and Jokat (2012) and Mueller and Jokat (2017) for the magnetic spreading anomalies in the Mozambique Basin, and on Goodlad et al. (1982) for the magnetic anomalies in the South Natal Valley. The outline of the Naude Ridge, the South and East Tugela Ridges are from Goodlad (1986). OBS and LSS locations from the MOZ3/5 experiment are indicated by circle and triangle, respectively. Stations along the MZ1 and MZ2 profiles are indicated in red, except those presented in the following article that are highlighted in yellow. AG, Ariel Graben; DP, Dana Plateau; *E*-TuR, East Tugela Ridge; GP, Galathea Plateau, Vauban Plateau; MG, Mazenga Graben; NNV, North Natal Valley; NR, Naude Ridge; SNV, South Natal Valley; S-TuR, South Tugela Ridge. (For interpretation of the references to color in this figure legend, the reader is referred to the web version of this article.)

and difficulties in interpreting magnetic anomalies along the margins. In the absence of modern deep seismic investigation, information on the age and nature of the underlying crust, their spreading regimes and constraints on first horizontal movements are still debated. Those uncertainities have resulted in varied data interpretations and model predictions based on different data sets, leading to diverse "tight-fit" reconstructions: for example König and Jokat, 2006; Eagles and König, 2008; Torsvik et al., 2012; Gaina et al., 2013; Nguyen et al., 2016; Davis et al., 2016) adopt a model pre-dominantly based on geophysical data (gravity and magnetic data); whereas the modeling of Tarling, 1972 and Powell et al., 1980 is based on onshore geological data, with less consideration of geophysical data. Thompson et al., 2019 summarize all these comparisons and finally propose a new fit.

2. Geological & tectonic background

Located in the south-east corner of Southern Africa, the Southern Mozambique Basin is an area flanked on the west and the north-west by pre-Palaeozoic structures: the Kaapvaal and the Zimbabwe Cratons, respectively (Fig. 1b). The external limits of this basin are defined by the succession of the north–south Lebombo monocline and the north-east to south-west Mateke-Sabi monocline (Salman and Abdulla, 1995). New deep seismic data acquired within the scope of the PAMELA project, provides key arguments for the existence of a thick continental crust in the MCP and NNV, in continuity to the cratons that were surrounding before the breakup, and which present a comparable velocity structure (Moulin et al., 2020; Leprêtre et al., 2020). Evain et al. (2021), Li et al. (2021) and Watremetz et al. (2021) detailled the Limpopo Margin (LM), eastward the MCP and the NNV, as an N—S strike-slip margin segmented by two major structures (LF and MFZ). The thinning domain reveals a continental nature in direct eastward prolongation of the continental crust that floors westwards, capped by pre-Neocomian volcano-sedimentary basin (Evain et al., 2021; Schnurle et al., 2023). In-between the LF and MFZ and before reaching the oceanic crust in the Mozambique Basin (MB), the Limpopo Corridor (LC) presents a domain of anomalous crust interpreted as a ductile shearing domain made of flowing lower continental crust intruded by intense magmatism (Evain et al., 2021; Fig. 2). The crustal thickness is extremely variable (5 to 15 km) and appears thicker to the south (MZ1) than to the north (MZ3, MZ4, MZ5). The LC is marked by high positive gravity anomalies in continuation of those produced by the Dana and Galathea Volcanic Plateaus. For that reason, these gravity anomalies were previously thought to be a part of volcanic Mozambique Ridge (for instance: Mueller and Jokat, 2017). Recent studies have shown however that these anomalies mark in fact the presence of large and thick contourite structures above a thin continental, intruded crust (Moulin et al., 2020; Evain et al., 2021; Li et al., 2021; Babonneau et al., 2022)

3. Data acquisition & processing

3.1. The MOZ3/5 experiment

The MOZ3–5 cruise of the integrated multidisciplinary PAMELA (PAssive Margin Exploration LAboratory), conducted by TOTAL, IFREMER, in collaboration with Université de Bretagne Occidentale, Université Rennes 1, Université Pierre and Marie Curie, CNRS et IFPEN, is located in the south-east corner of Southern Africa. New geophysical and geological data was acquired onboard the R/V *Pourquoi Pas?*, from February 11th to April 4th 2016, on the southern-Mozambique and Limpopo margin (Fig. 1a & 1b). Seven coincident wide-angle seismic (WAS) and Multi-Channel Seismic (MCS - 720 traces) profiles were collected with 193 deployments of Ocean Bottom Sismometers (OBS) from Ifremer's Marine Geosciences pool (Auffret et al., 2004), as well as gravitmetric, magnetic, bathymetric, cored, dredged, sub-bottom profiles and water column data (Moulin and Aslanian, 2016; Moulin and Evain, 2016). Simultaneously, 124 Land Seismic Stations (LSS) were deployed in Mozambique, extending six of those profiles on land for about 100 km in order to provide information on the onshore-offshore transition (Figs. 1 and 2). The seismic source was composed of 15 air-guns providing a total volume of 6500-in^3, with a shot interval set at 60 s. Along MZ1 and MZ2 profiles presented here, a total of respectively 3241 and 11,792 air-gun shots were generated and recorded jointly by OBS, LSS and a marine streamer. 38 OBSs spaced every ~12.5 km were deployed along the 545 km long WNW-ESE oriented MZ1 profile, at water depths of 210 to 4560 m. 110 km northwards and parallel to the MZ1, MZ2 is 300 km long and covered by 33 OBSs at water depths of 385 to 2022 m. Inland, 16 and 19 LSS (Reftek 125A-01 and L-4C) were deployed along MZ1 and MZ2, respectively, at altitudes ranging from 5 to 144 m. Inter-station distance of 5 km results in a landward extension of these profiles of about 100 km for MZ1 and 120 km for MZ2.

3.2. MCS data processing

The MZ1 and MZ2 profiles were acquired without any major problem. A first quality control and pre-processing was undertaken on the reflection seismic data using the *SISPEED* software (Ifremer), and further processing of the MCS data was then performed using the *GEOCLUSTER* software (CGG Veritas). The processing sequence was composed of geometry, wide butterworth frequency filter (2–12–64-92 Hz), resample traces from 2 ms to 4 ms, spherical divergence compensation, deconvolution, Common Mid Point (CMP) sorting, water-bottom multiple attenuation, frequency filter (2–12–48-64 Hz), surface-related multiple modeling and attenuation, editing and water column mute, velocity analysis, Kirchoff pre-stack time migration, update of the velocity analysis, normal move-out correction, multiple attenuation in the radon domain, dip move-out, CMP stacking, F-k migration and, Kirchoff post-stack time migration (PSTM).

3.3. Wide-angle data processing

Pre-processing of OBS data included internal clock-drift correction to the GPS base time, and correction of instrument's positions at the seafloor using the direct water wave to take into account the drift during their descent. We applied upward and downward traveling waves separation processing (e.g. Schneider and Backus, 1964) by combining hydrophone and vertical seismometer OBS components. It includes a spiking predictive deconvolution of the upward traveling record using the downward traveling wave as signature. Spherical divergence is calculated to compensate amplitude decay of the records and traces are further scaled with a gain proportional to the offset in order to enhance the refracted events.

LSS's records were first debiased and band-pass filtered and stacked by arrays. In addition, the LSS data were reduced by an 8.0 or 8.5 km/s velocity, which flatten the principal Pn arrivals and then processed with an FX deconvolution (in a moving 1.9 s × 21 traces window) to attenuate random noise. A gain equal to the offset was finally applied to enhance the refracted events.

4. Data analysis

4.1. Modeling approach and generalities

From the seismic data-sets presented above travel-times picks were extracted in order to built a P-wave velocity model along both MZ1 and MZ2 profiles. We applied an iterative procedure of two-dimensional forward ray-tracing using the RAYINVR software (Zelt and Smith, 1992). Modeling was performed following a layer-stripping strategy, proceeding from top (seafloor) to bottom (Moho and mantle) adjusting for each layer velocity and interface-depth nodes such as to minimize the difference between observed/picked arrival times and computed ones in the model. Initial models included a water layer where seafloor bathymetry was taken from multibeam data acquired during the MO3/5

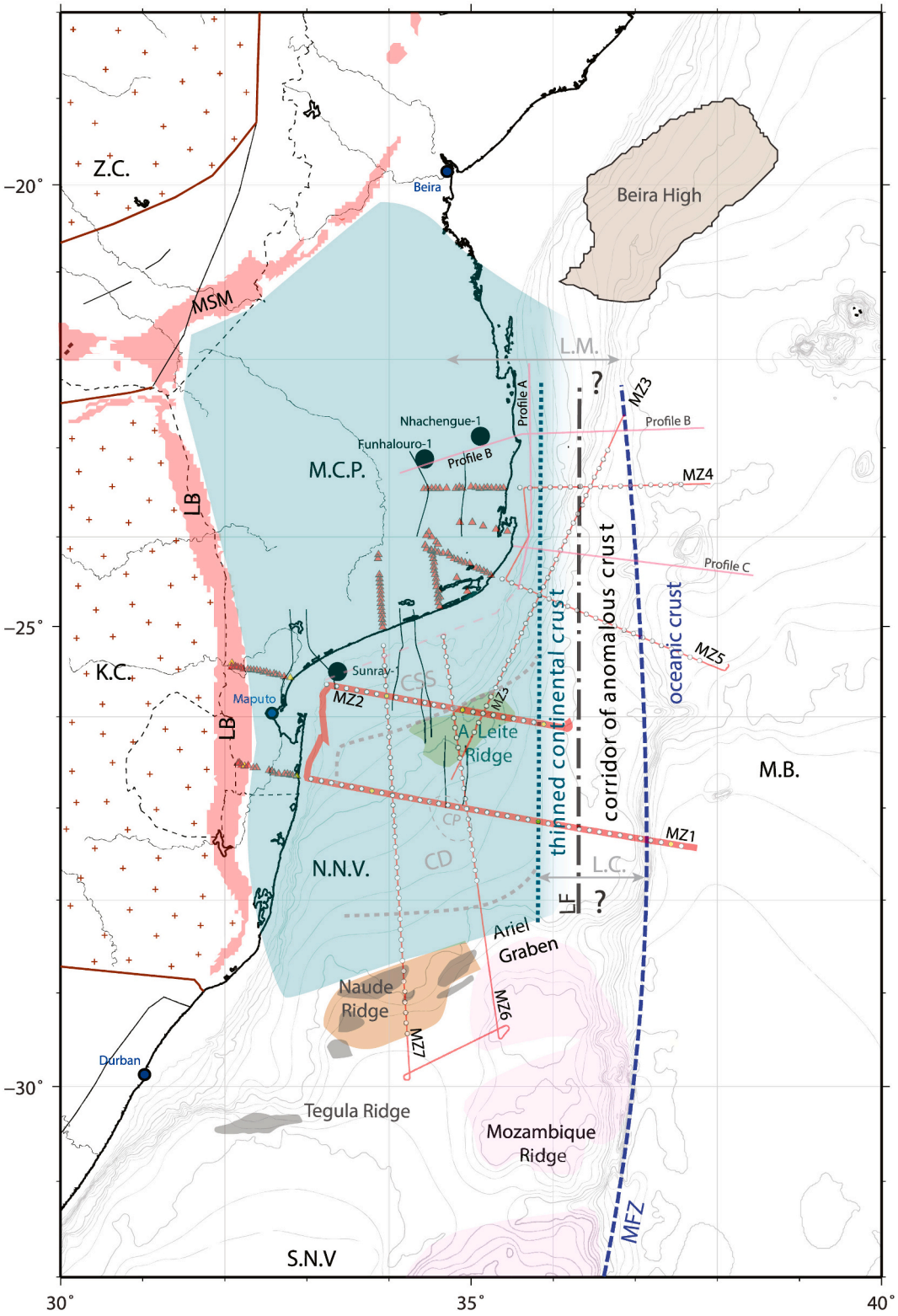

Fig. 2. : Map of the main segmentation and boundaries area resulting from the combined interpretation of PAMELA-MOZ35 deep seismic profiles, modified from Evain et al., 2021. Pink lines are locations of line drawings of commercial MCS profiles used by Evain et al., 2021 and Schnurle et al., in press. The background shows the main geological units and structures on land: KC stands for Kaapval Craton, LB stands for Lebombo monocline, MSM stands for Mateke Sabi Monocline, MCP stands for Mozambique Coastal Plain, NNV stands for North Natal Valley, and ZC stands for Zimbabwe Craton. Offshore bathymetric contours in the LM are as follows: Limpopo margin (LM), Mozambique Basin (MB) and South Natal Valley (SNV). The main geological features are as follows: Continental Shelf and Slope (CSS), Central Domain (CD), Central Plateau (CP), Almirante Leite Ridge (ALR), Beira continental block or high (BH), Limpopo Fault (LF), Mozambique Ridge (MR), Mozambique Fracture Zone (MFZ), Tegula and Naude ridges, and Ariel Graben (AG). MOZ35 seismic acquisition in the NNV and LM is shown in red, with MZ1 and MZ2 profiles highlighted with a bold red line. (For interpretation of the references to color in this figure legend, the reader is referred to the web version of this article.)

cruise and onshore topography extracted from GEBCO. Arrival times of the main sedimentary interfaces (*see below* part 4.2.1) up to the acoustic basement (*see below* part 4.2.2) were picked from the coincident MCS line and integrated in the modeling, as long as they are correlated with identified phases in the OBS data to avoid over-parameterization of the model. We further checked the coherence of our velocity models against MCS data by converting the former from depth to two-way-travel-time (twt). Beyond the acoustic basement (*see below* parts 4.2.3 and 4.2.4), we used only arrival times picked from OBS and LSS records keeping velocity models minimal, i.e. inserting lateral topographic and velocity changes only where required by the data.

The quality of MCS data (MZ1 and MZ2) is generally good, even if seismic signal does not image beyond 2.5–3.5 s twt below the seafloor, partly due to the presence of numerous multiples from the seafloor and other major interfaces in the stratification, as well as probable high velocity layers (such as carbonate and/or volcanic layers) (Fig. 11).

With respect to OBS and LSS data, their quality is also globally very good. Examples of LSS recorded sections are shown in Figs. 3 and 4 while some OBS records are presented in Figs. 5 to 10. Note that MZ2LSS06 and MZ2LSS15 to MZ2LSS20 present very noisy records probably due to poor coupling induced by the nature of the soil. Also, because MZ2LSS12 to MZ2LSS14 records were interrupted they were not used in the modeling. As for OBS records they show blind zones at shots made above the volcanic edifices of the Almirante Leite Ridge (ALR).

Based on analysis of the P-wave seismic velocity variations, the study area was subdivided into five domains:

1) The onshore domain of the MCP where LSS were deployed.
2) The Continental Shelf and Slope (CSS), between −50 and 30 km model-distance on MZ1 and 0–160 km model-distance on MZ2;
3) the Central Domain (CD), between 40 and 270 km model-distance on MZ1 and 160 to 220 km model-distance on MZ2, dominated by the ALR;
4) the Limpopo Corridor (LC), at the extremity of MZ2 (230 to 260 km model-distance) and from 280 to 410 km model-distance on MZ1;
5) the Mozambique basin (MB) from 420 to 450 km model-distance on MZ1 only.

4.2. Input model setup

MZ1 velocity model is composed of 7 sedimentary and 2 volcano-sedimentary layers, 4 crustal layers and 2 mantle layers. MZ2 was modeled with 6 sedimentary layers and also 2 volcano-sedimentary layers, 4 crustal layers including a layer of anomalous high velocity separated from a single layer of mantle by a highly reflective interface (Figs. 11, 12A and 13A). In the sections below, we explain how these choices were made.

4.2.1. Upper sedimentary and volcanic layers

Sedimentary deposits are highly heterogeneous along our two profiles with the CSS and LC representing two domains of major accumulation (Fig. 11).

Over the CSS, sediments are up to 2 s twt thick but present contrasting structures and facies between profiles. On MZ1, layers S1 and S2 are poorly resolved and appear transparent. On OBS records, Ps1 refracted arrivals are observed on a very short offset range with apparent velocities round 1.6–1.7 km/s. Generally, along our profiles, Ps1 can be hard to identify due to their short offset range and low apparent velocities (1.6–1.7 km/s). The layer S1 is mainly introduced for forward modeling purposes, to allow better fit of reflected and refracted arrivals of the underlying S2 layer. S2 is better constrained by refracted arrivals with apparent velocities higher than 2.0 km/s. S3 (2.3–2.5 km/s) and S4 (2.2–2.4 km/s) highlights strong reflectors within the sedimentary sequence. The underlying S5 (2.25–2.45 km/s) and S5b (3 km/s) layers are only visible along western continental shelf where they pinch-out at 25 km and 44 km model-distance, respectively and are required by wide-angle data on the 3 last OBS (OBS36-0BS38). Finally S6 (3.25–3.75 km/s) lies directly above the bright top of the acoustic basement and presents strong internal stratification (in green on Fig. 11-MZ1a). On MZ2, only 6 layers were modeled. Below the uppermost layer S1, S2 and S6 present strong internal and coherent stratification. S2 is characterized by long offset refracted phase of apparent velocity between 2.0 and 2.9 km/s with a positive gradient eastward. From MZ2OBS01 (Fig. 8) to MZ2OBS07 the Ps4 refracted phase is well recorded with velocities around 3 km/s, however it becomes absent from records further east suggesting a velocity inversion. Layer S6 is limited to the transition between the CSS and the CD and highlights high velocity, probably magmatic, lenses inter-bedded within the sedimentary sequence. On wide-angle records they show up with high apparent velocities (4.3 to 4.9 km/s) refracted phases on MZ2OBS14 -MZ2OBS16 (Fig. 9).

In the CD of MZ2 profile, the two sedimentary layers of our model are strongly perturbed by volcanics from the ALR. The Ps1 apparent velocity increases to 1.85 km/s but the layer S1 pinches out between MZ2OBS17 and MZ2OBS18. The facies of S2 becomes transparent and apparent velocities on OBS sections for the Ps2 phase increase to 3.0–3.7 km/s. On MZ1 profile, the CD forms an almost flat and high plateau at the center of the NNV with the acoustic basement locally reaching the seafloor. Its topography alternates between horsts and grabbens. Sedimentary infilling within grabens reach a maximum thickness of 1.0 s twt where three layers at most were modeled. The layers are relatively well bedded, with apparent velocity slower than CSS (around 2.0 km/s). By contrast, high velocities close to 5 km/s are recorded directly below the seafloor at the morphological high located at the intersection with the MZ6 profile.

The eastern extremity of MZ2 profile reaches the LC where the sedimentary sequence thickens. Below layer S1, the interface between S2 and S3 marks a change in facies, which is almost transparent in S2 while clear and continuous stratification are visible in S3 (Fig. 11-MZ2). Velocities here are mostly constrained from MZ2OBS23 (Fig. 10) on which Ps2 and Ps3 ave. respectively 2.0–2.2 km/s and 2.8 km/s km/s apparent velocities. On MZ1, the entire sedimentary structure of the LC is imaged up the MFZ where it ends abruptly (Fig. 11-MZ1b). The area was previously recognized as a host of major contourite deposits and complex tectonic history (e.g. Li et al., 2021; Babonneau et al., 2022). Five layers (S1, S3, S5, S6 and S7) were modeled and selected to highlight similar velocity ranges in the CSS (layers S2 and S4 are thus absent). On OBS data, the phases that characterized this layer appear as a fan of secondary arrivals recorded between ~4.5 and 20 km. Below S1, S3 layer corresponds to the sedimentary body between 365 and 405 km model-distance characterized by a refracted phase of 2.3 k/s apparent velocity on MZ1OBS08 to MZ1OBS05 records. Elsewhere, beneath S1, the S5 layer that extends from the eastern part of the CD is constrained by a strong undulating reflector at its roof and refracted phases of apparent velocities increasing eastward from 2.0 km/s (MZ1OBS13) up to 2.75 km/s (MZ1OBS08-MZ1OBS05). For the layer below, a Ps6 phase is identified with apparent velocities of 2.75 km/s with a local maximum of 3.0–3.1 km/s between MZ1OBS08 and MZ1OBS06. Layer S7 is draping the acoustic basement of the LC and constrained from clearly visible Ps7 refracted phases on OBS (MZ1OBS11-MZ1OBS07) sections that show apparent velocities of 3.25–3.50 km/s. In addition, all the present S layers pinch-out eastwards on the peak localized at the MZ1OBS04, associated with the MFZ.

Finally, east of the MFZ, the extremity of MZ1 runs over the MB (between 420 and 475 km model-distance on Fig. 11-MZ1b). Here sediments thickness is up to 1.25 s twt and relatively well-bedded.

4.2.2. Acoustic basement and volcano-sedimentary layers

From the CSS to the MB, a pronounced high amplitude, low frequency reflector identifies the acoustic basement, except on the westernmost part of MZ1where this signal is lost. This basement marks the top of two volcano-sedimentary layers and reaches the seafloor at two location: MZ1OBS22 and the MFZ. The upper SV1 layer still shows some

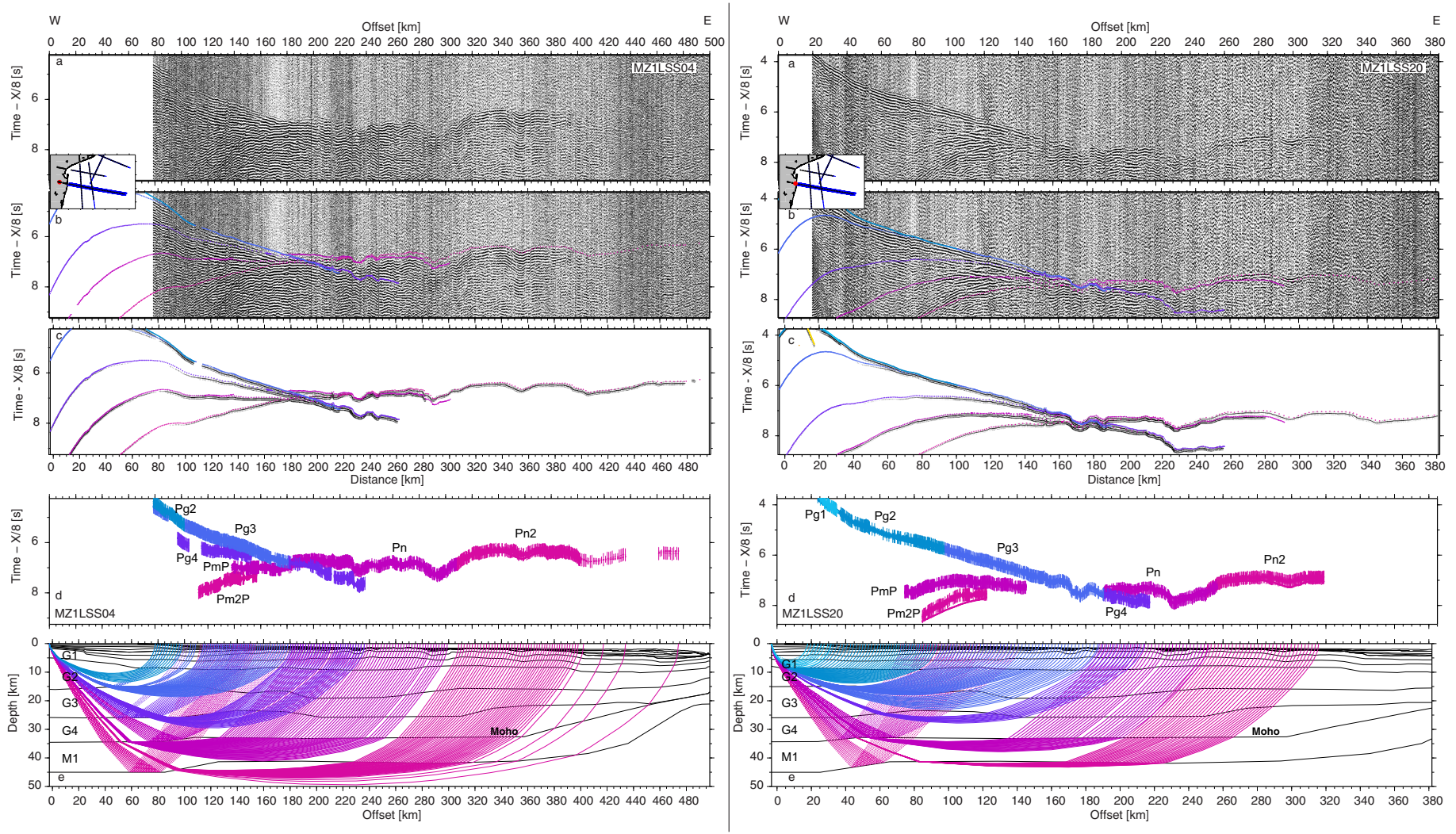

Fig. 3. : Left: MZ1LSS04 – Focus on the crust and mantle at positive offsets (toward the E). a) Seismic record; b) Seismic record with color coded predicted travel-times overlain; c) Color coded synthetic; d) Color coded observed travel-times (vertical bars, the size showing the uncertainty range), overlain by color coded predicted travel-times (color dots); e) Seismic rays. On a, b, c, and d, travel-times is reduced by a velocity of 8.0 km/s. Right: MZ1LSS20 – Focus on the crust and mantle at positive offsets (toward the E). a) Seismic record; b) Seismic record with color coded predicted travel-times overlain; c) Color coded synthetic; d) Color coded observed travel-times (vertical bars, the size showing the uncertainty range), overlain by color coded predicted travel-times (color dots); e) Seismic rays. On a, b, c, and d, travel-times is reduced by a velocity of 8.0 km/s.

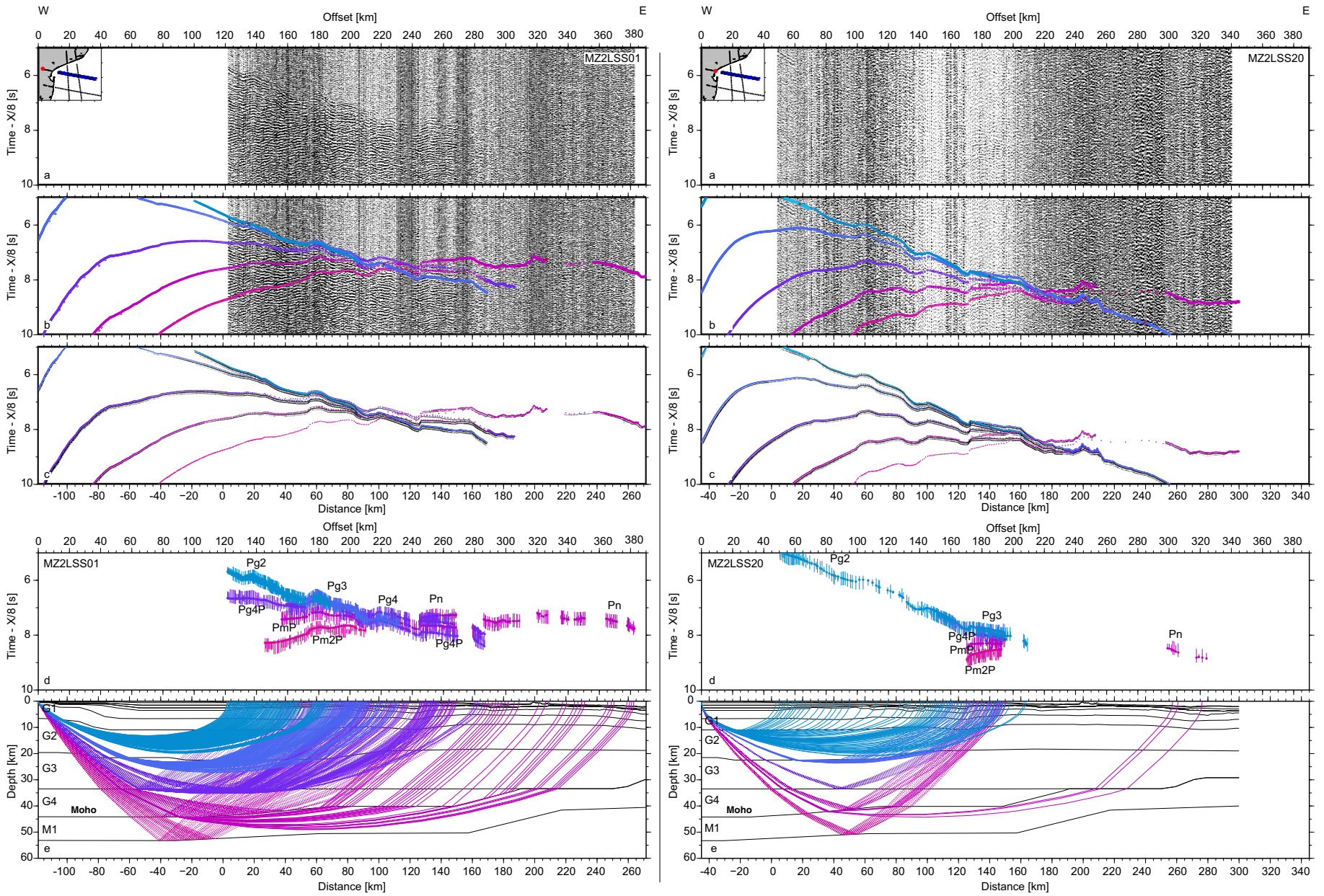

Fig. 4. : Left: MZ2LSS01 – Focus on the crust and mantle at positive offsets (toward the E). a) Seismic record; b) Seismic record with color coded predicted travel-times overlain; c) Color coded synthetic; d) Color coded observed travel-times (vertical bars, the size showing the uncertainty range), overlain by color coded predicted travel-times (color dots); e) Seismic rays. On a, b, c, and d, travel-times is reduced by a velocity of 8.0 km/s. Right: MZ2LSS20 – Focus on the crust and mantle at positive offsets (toward the E). a) Seismic record; b) Seismic record with color coded predicted travel-times overlain; c) Color coded synthetic; d) Color coded observed travel-times (vertical bars, the size showing the uncertainty range), overlain by color coded predicted travel-times (color dots); e) Seismic rays. On a, b, c, and d, travel-times is reduced by a velocity of 8.0 km/s.

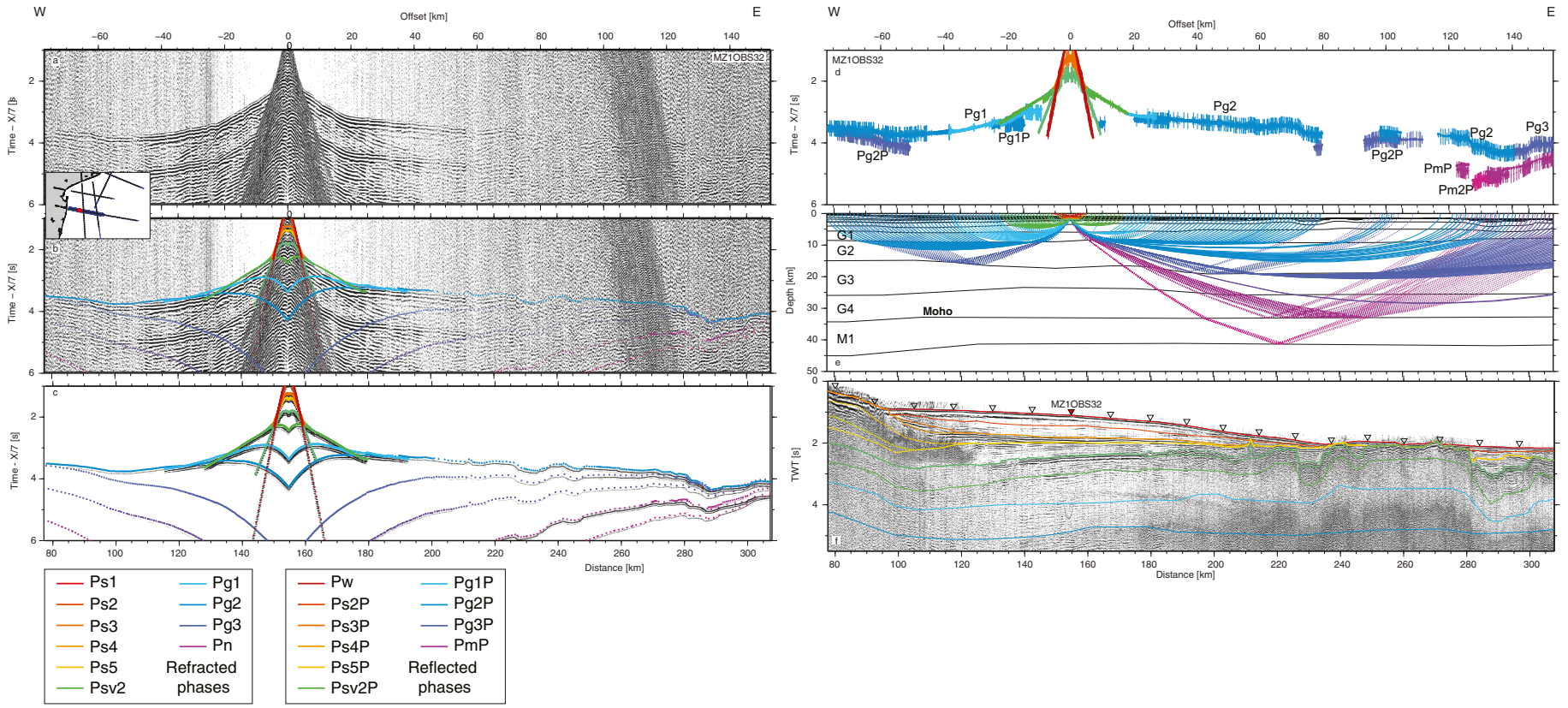

Fig. 5. : MZ1OBS32 – Focus on the crust and mantle at both negative and positive offsets. a) Seismic record; b) Seismic record with color coded predicted travel-times overlain; c) Color coded synthetic; d) Color coded observed traveltimes (vertical bars, the size showing the uncertainty range), overlain by color coded predicted travel-times (color dots); e) Seismic rays; f) MCS time migrated section and color coded model interfaces. On a, b, c, and d, travel-times is reduced by a velocity of 7.0 km/s.

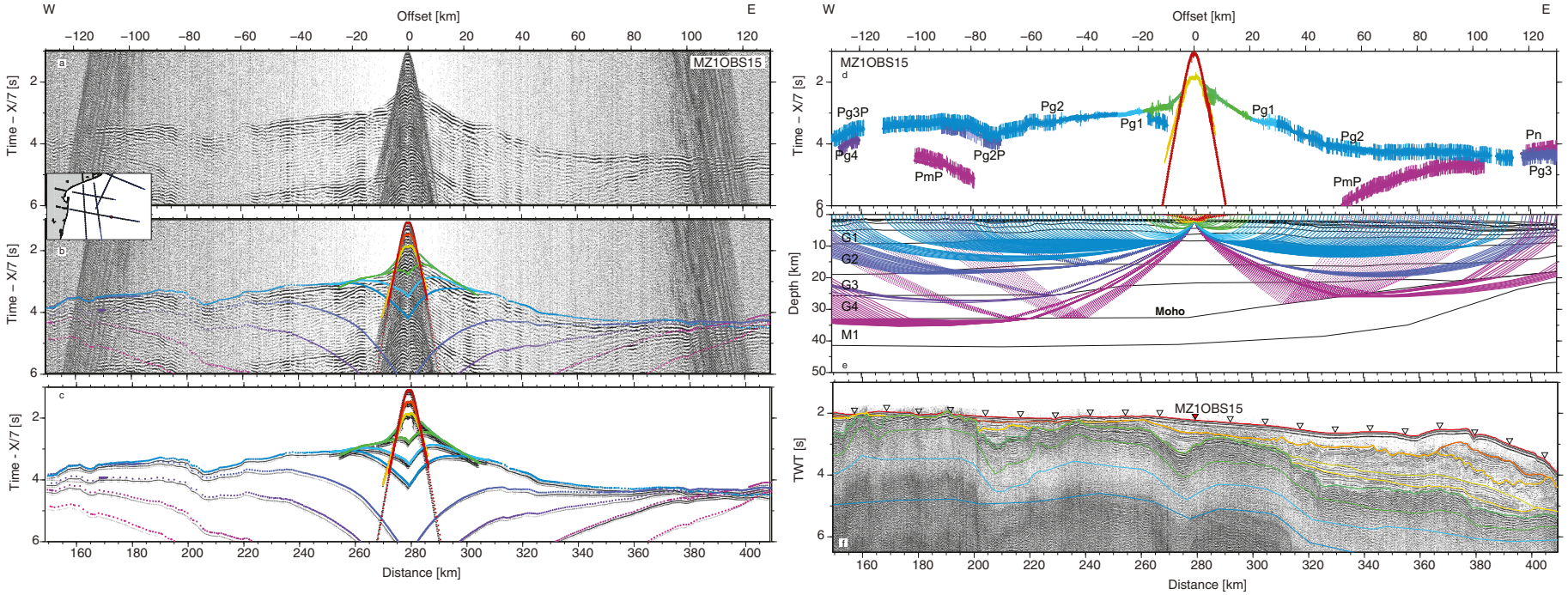

Fig. 6. : MZ1OBS15 – Focus on the crust and mantle at both negative and positive offsets. *Same legend and color code as* Fig. 5.

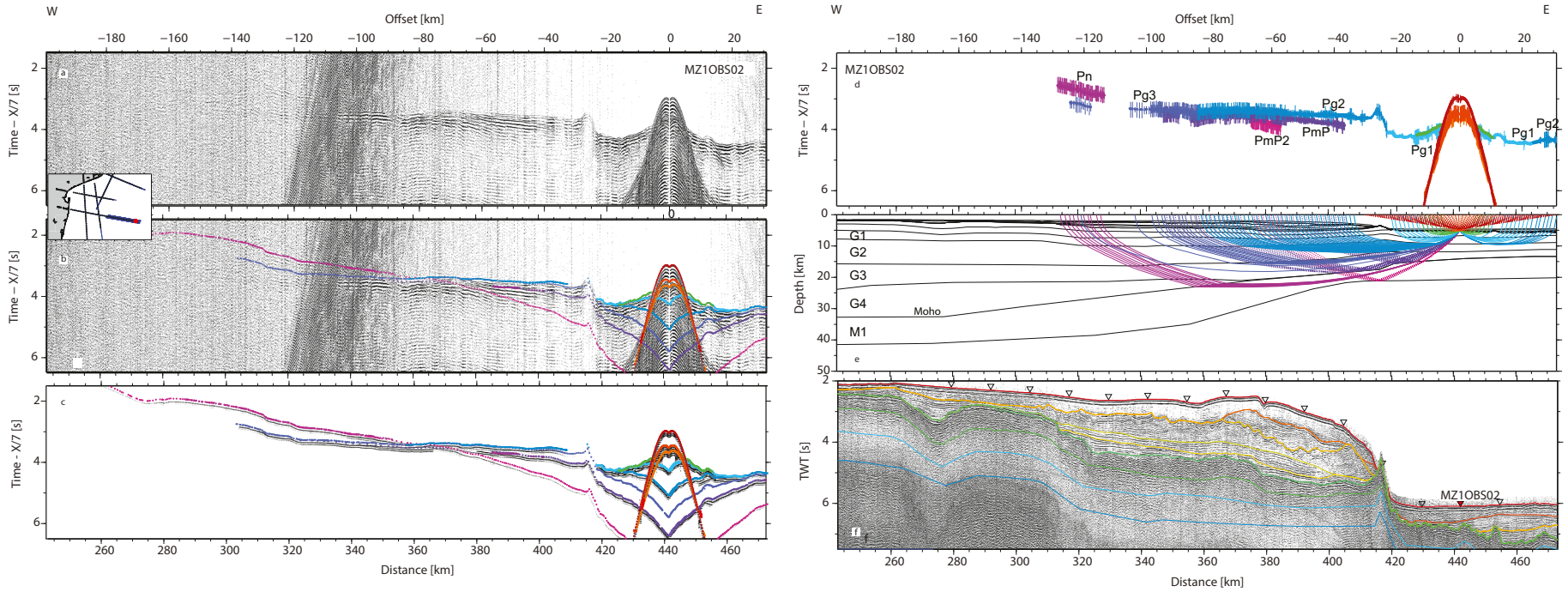

Fig. 7. : MZ1OBS02 – Focus on the crust and mantle at both negative and positive offsets. *Same legend and color code as* Fig. 5.

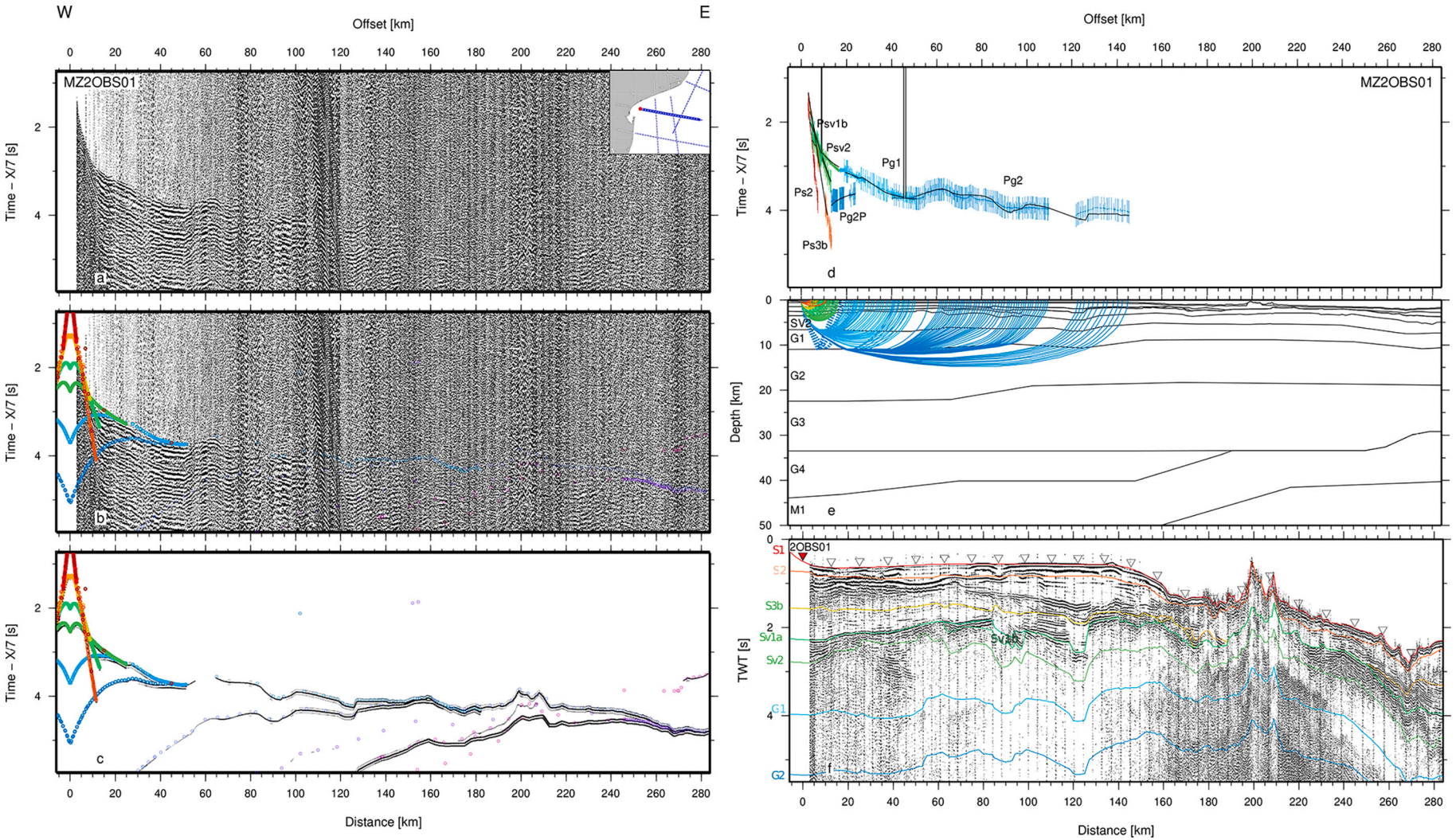

Fig. 8. : MZ2OBS01 – Focus on the crust and mantle at both negative and positive offsets. *Same legend and color code as* Fig. 5.

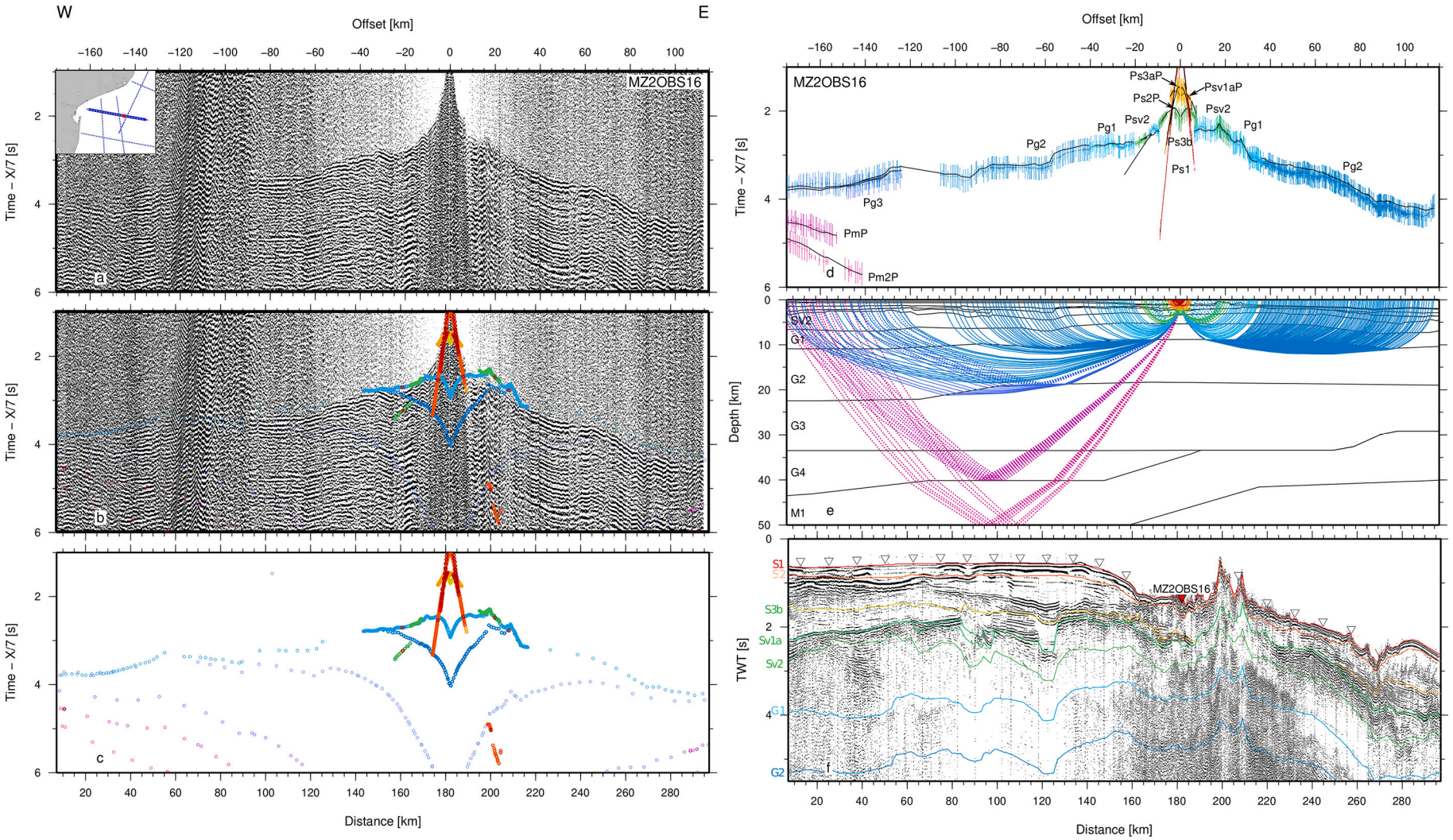

Fig. 9. : MZ2OBS16 – Focus on the crust and mantle at both negative and positive offsets. *Same legend and color code as* Fig. 5.

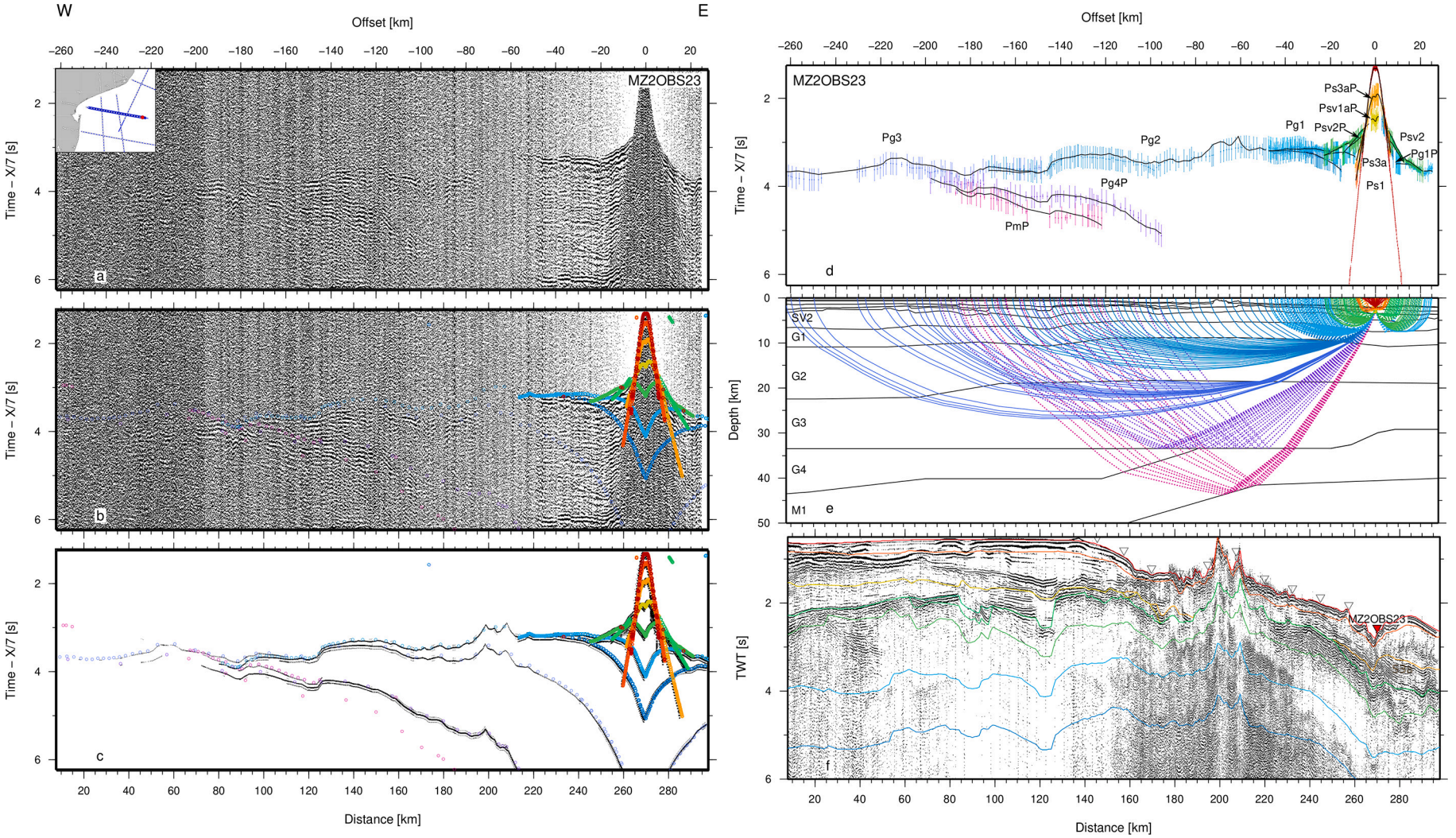

Fig. 10. : MZ2OBS23 – Focus on the crust and mantle at both negative and positive offsets. *Same legend and color code as* Fig. 5.

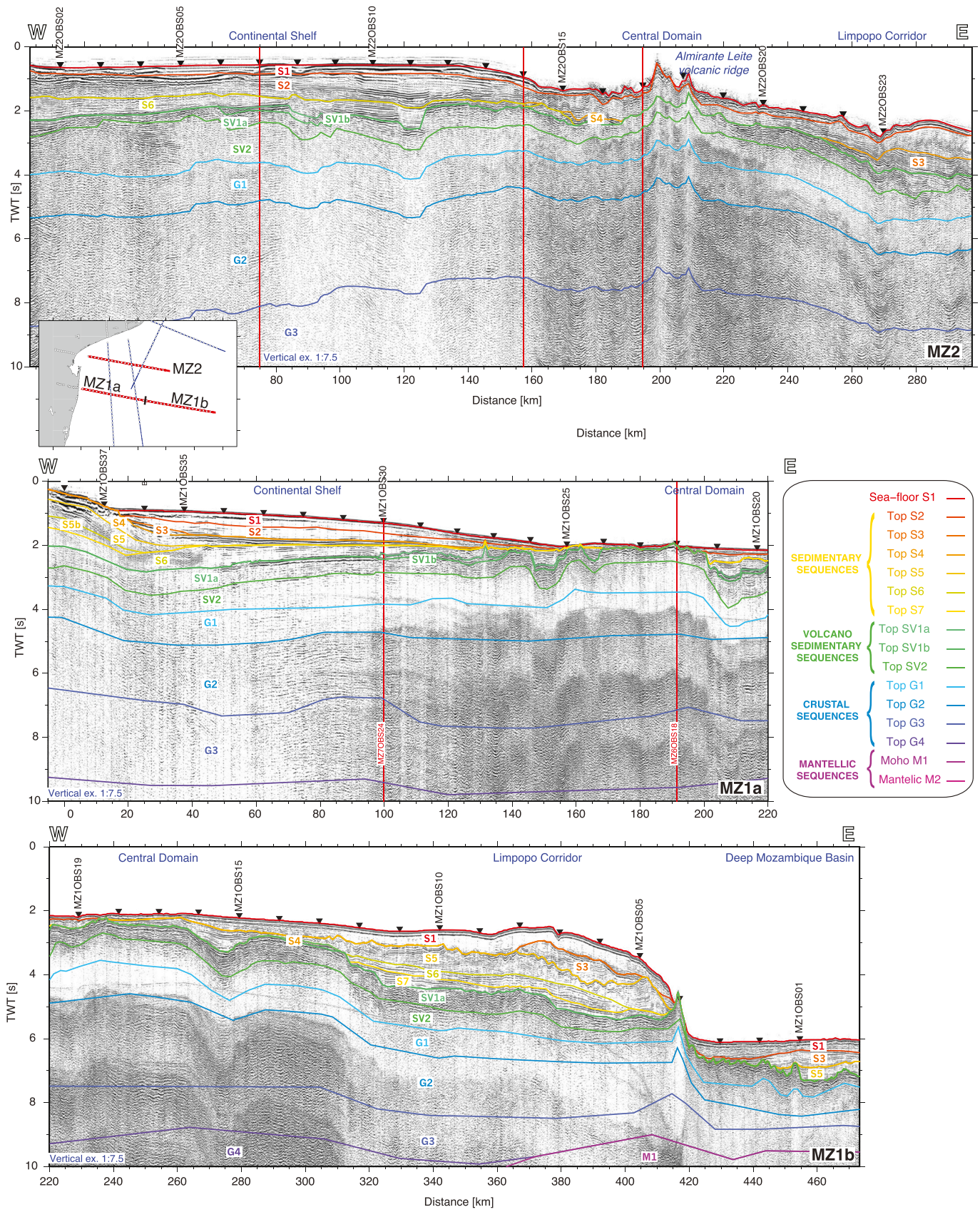

Fig. 11. : Insert of MOZ3/5 dataset (blue lines), MZ1 and MZ2 profiles are indicated by red lines. OBS and LSS locations are indicated by white circles. A) two-way travel-time record section of MCS data along MZ2 profile overlain by time converted interfaces of wide-angle model MC2, B) Zoom on the western part of the two-way travel-time record section of MCS data along MZ1 profile overlain by time converted interfaces of wide-angle model MC1. C) Zoom on the eastern part of the two-way travel-time record section of MCS data along MZ1 profile overlain by time converted interfaces of wide-angle model MC1. Vertical exaggeration at seafloor is 1:7.5. (For interpretation of the references to color in this figure legend, the reader is referred to the web version of this article.)

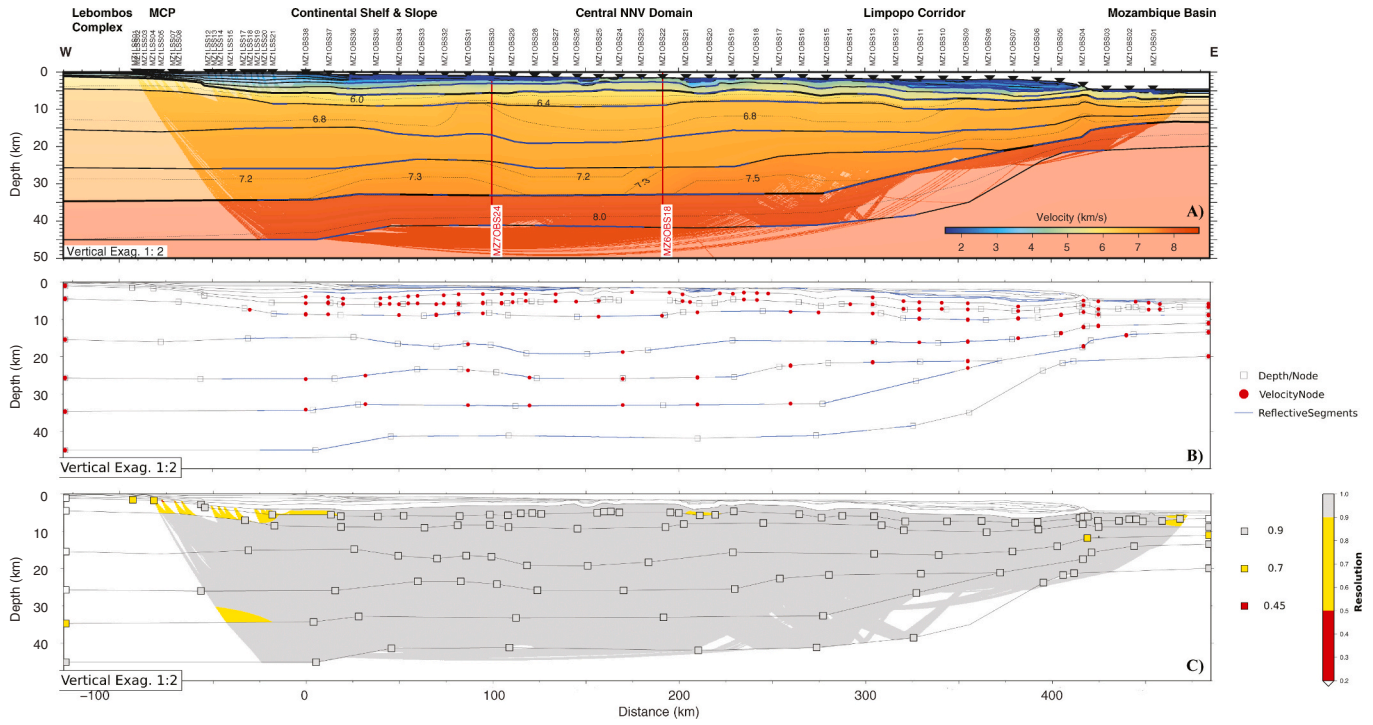

Fig. 12. : Final velocity model for the MZ1 profile and evaluation of the wide-angle model. (a) Final MZ1 velocity model. Thick blue lines indicate interfaces constrained by wide-angle reflections. Shaded areas indicate ray-coverage. (b) Model parameterization, including interface depth nodes (squares), top and bottom layer velocity nodes (red circles). Interfaces where reflections have been observed on OBS/LSS data are highlighted in blue. (c) Resolution of velocity (gridded and colored) and depth nodes (colored squares). Zones that were not imaged are blanked. MCP, Mozambique Coastal Plain; NNV, North Natal Valley. (For interpretation of the references to color in this figure legend, the reader is referred to the web version of this article.)

internal layering although discontinuous on the MCS profiles (Fig. 11). Below, SV2 appears mostly transparent because seismic signal is lost at these depths. On OBS records, because of its strong impedance contrast, reflected arrivals from the acoustic basement can be clearly identified except again on the western CSS as the reflector is absent and on few OBS records located over the LC (e.g. MZ1OBS11-MZ1OBS09). The two SV layers are also well characterized by refracted first arrivals between 5 and 20 km offsets generally and over the whole profiles. Those have apparent velocities ranging from 4 to 6 km/s going down to 3.5–4.75 on the western CSS. The SV1 layer in our models is subdivided in two (SV1a and SV1b) because locally we modeled thin layer at the acoustic basement. This is justified by the presence of shadow zones on few OBS records (e.g MZ2OBS07) suggestive of velocity inversions in the layer SV1. The contrast is less sharp between SV1 and SV2 throughout the profiles but still some reflected arrivals were identified and used to constrain the depth of this interface.

4.2.3. *Crystalline crustal layers*

Crustal layers were solely constrained from seismic OBS and LSS data. For both profiles fours layers (G1-G4) were necessary, although only three layers (G1-G3) are used in the LC and MB domains. On OBS and LSS records, crustal refracted phases are well observed continuously over long offsets, 200–215 km on average for OBS (Figs. 5 to 10) and up to 480 km offsets for LSS (e.g. MZ1LSS04: Fig. 3a). Arrivals from the upper crustal layer (G1) seem to have been recorded on OBS and only at LSS located close to the the coast (MZ1LSS17 to MZ1LSS21 Fig. 3b). These phases show apparent velocities around 5.75–6.00 km/s on the MCP and CSS increasing eastwards to 6.25–6.75 km/s in the LC and MB. Phases associated with deeper crustal layers (G2, G3 and G4) are recorded by almost all the instruments. Their arrivals have increasing apparent velocities in the range of 6.8–7.0 km/s in layer G2, 7.0–7.1 km/s in layer G3. Apparent velocities for layer G4 are higher than 7.0 and can reach 7.5 km/s. The corresponding refracted phases including some secondary arrivals are less evident on records.

Despite limited velocity jumps between crustal layers, reflected phases (PgP) are numerous on LSS and OBS records, which clearly suggests important internal layering. To avoid adding complexity in our models we did not exploit all these arrival times limiting the number of interfaces, which are thus only partly sampled.

4.2.4. *Moho interface and Mantle layers*

As for crustal phases, the reflected phase at the Moho (PmP) and reflected arrivals in the mantle are clearly identified on both LSS and OBS records. The prolongation at depth of internal heterogeneity or layering within the upper mantle is attested from evidences of high amplitude package of reflections, particularly on stations close to the coast (Figs. 3b and 7).

The triplication of reflected and refracted phases at the crust/mantle interface may provide clue on crustal thickness. For LSS and OBS located over the CSS it is located at offsets larger than 150 km suggesting thick crust. Toward the east, the offset distance of the crust/mantle phase triplication decreases progressively in the CD then more abruptly in the LC to reach 60 km offset (Figs. 6 to 10). In the MB, triplication occurs at $<$50 km offset.

Pn refracted arrivals from the mantle are more weakly recorded on OBS than LSS; they were not identified, for instance, on all MZ2OBS records and between MZ1OBS28 to MZ1OBS18. Two refracted phases (Pn1 and Pn2) in the mantle are generally of high amplitude, where the crust becomes thinner. These phases show apparent velocities around 8.0 km/s or slightly higher.

5. Forward model and evaluation

5.1. *Error analysis*

From MZ1 and MZ2 OBS and LSS records, we extracted 155,002 and

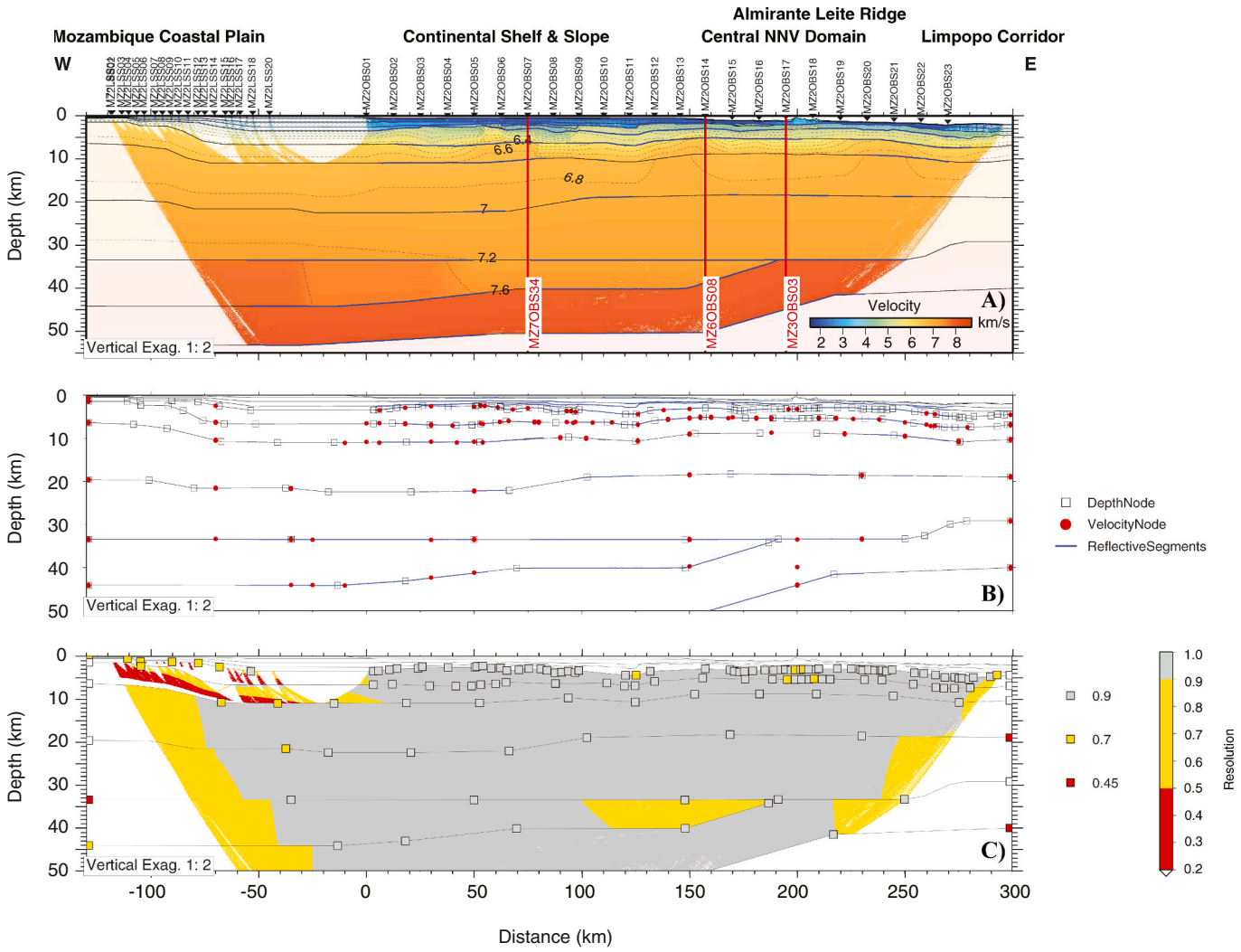

Fig. 13. : Final velocity model for the MZ2 profile and evaluation of the wide-angle model. (a) Final MZ2 velocity model. Thick blue lines indicate interfaces constrained by wide-angle reflections. Shaded areas indicate ray-coverage. (b) Model parameterization, including interface depth nodes (squares), top and bottom layer velocity nodes (red circles). Interfaces where reflections have been observed on OBS/LSS data are highlighted in blue. (c) Resolution of velocity (gridded and colored) and depth nodes (colored squares). Zones that were not imaged are blanked. MCP, Mozambique Coastal Plain; NNV, North Natal Valley. (For interpretation of the references to color in this figure legend, the reader is referred to the web version of this article.)

43,078 arrivals, respectively and interpreted their corresponding phases (Tables 1 and 2). Travel-time uncertainty was computed from the ratio of signal energy (in a 20 ms window) to average energy in the 68 ms preceding the signal according to Zelt and Forsyth (1994). The uncertainty ranges from 0.020 s (MZ1) - 0.025 s (MZ2) for high ratio to 0.25 s for poor ratio. Our final models explain 151,455 arrival times or 98% of total picks, with a global RMS residual of 0.069 s for MZ1. For MZ2 41,277 arrivals are explained or 96% of total picks, with a global RMS travel-time residual of 0.062 s. Given our uncertainties, the two models result in a normalized chi-squared of 0.591 for MZ1 and 0.43 for MZ2 (Tables 3 and 4). For both lines crustal arrivals represent >50% of total picks.

5.2. *Indirect model evaluation*

Interface depth node spacing as well as velocity node spacing is key to model the lateral variations of the seismic velocity with sufficient resolution, but without introducing complexity not required by the data (Zelt, 1999). Figs. 12 and 13 present three indicators of model quality for MZ1 and MZ2 profiles, respectively. The top panel (Fig. 12A and 13B) represents the final velocity model, indicating in thick blue lines where the interfaces are constrained by wide-angle reflections. The middle panel (Figs. 12B and 13B) represents the parameterization of the velocity models with the depth and velocity nodes, and the reflective segments at interfaces. The bottom panel (Figs. 12C and 13C) shows the resolution parameter.

For both profiles, depth and velocity nodes defining the sedimentary and volcano-sedimentary are densely spaced since they are constrained and controlled by coincident MCS data. Hence, we truly started our evaluation for velocity nodes characterizing the SV2 layer. All indicators of model quality are calculated for all velocity and depths nodes in the crust and the upper mantle. Those nodes are not spaced evenly but located where they are required to allow good fit of arrivals. Thus, the overall node spacing tends to progressively increase with depth with loss of resolution by the wide-angle data. There is also a decrease of node spacing eastward where the crust becomes thinner and local variations in the structure are better appreciated. Typically, resolution matrix diagonals >0.5–0.7 are said to indicate reasonably well-resolved model parameters (e.g. Lutter and Nowack, 1990). The major part of the interface and velocity nodes present good resolution (>0.7) on both profiles (Fig. 12C and 13C). Resolution is poorest at the edges of our models. For MZ2 resolution decrease west of MZ2OBS01 below the MCP and CSS, and at the eastern tip eepest crustal layer (G4). The deepest mantle layer (M2) is generally parallel to the Moho with very large km

Table 1
Summarizes reflected or refracted phase name, number of explained events, residual mean-square, and normalized chi-squared value for MZ1 profile MZ1

Phase	Index	Npts	Trms (s)	Chi-squared
Pw	1	6146	0.033	0.623
Ps1	2	219	0.011	0.091
Ps2P	3	1106	0.044	0.136
Ps2	4	463	0.034	0.571
Ps3P	5	1280	0.066	0.498
Ps3	6	276	0.022	0.621
Ps4P	7	337	0.070	0.206
Ps4	8	231	0.019	0.756
Ps5P	9	517	0.050	0.309
Ps5	10	845	0.023	0.696
Ps6P	11	1190	0.051	0.562
Ps6	12	665	0.025	0.309
Ps7P	13	1071	0.029	0.139
Ps7b	14	1136	0.022	0.376
Psv1aP	15	2705	0.043	0.347
Psv1a	16	179	0.031	0.574
Psv1bP	17	291	0.034	0.464
Psv1b	18	1540	0.030	1.312
Psv2P	19	1203	0.048	0.580
Psv2	20	4536	0.066	2.220
Pg1P	21	3127	0.059	0.545
Pg1	22	8062	0.043	0.790
Pg2P	23	1699	0.063	0.522
Pg2	24	34,585	0.054	0.260
Pg3P	25	7054	0.086	0.457
Pg3	26	16,226	0.068	0.322
Pg4P	27	8965	0.069	0.284
Pg4	28	8539	0.068	0.301
Pm1P	29	13,906	0.089	0.607
Pn1	30	10,339	0.070	0.350
Pm2P	31	8333	0.145	1.604
Pn2	32	5697	0.152	2.050

node spacing in order to simply homogenize the velocity gradient in the upper mantle.

5.3. Uncertainty estimation using VMONTECARLO

We assess the reliability and uniqueness of our final models in the crustal and mantle layers by exploring randomly their parameter space using VMONTECARLO (Loureiro et al., 2016; Figs. 14 and 15). Depth nodes at the top of the crust are kept fixed during the search while those defining layers G2, G3, G4 and M1 (Moho) can randomly move vertically. Velocity nodes are allowed to vary from the top of layer G1 to the base of the upper mantle layer M1. This represents a total of 115 depth nodes and 134 velocity nodes for MZ1 while there are 52 and 87 respectively on MZ2.

For MZ1, fifty thousand random models were generated with maximum velocity variations at each node of ±0.4 km/s and maximum depth variations of ±1.0, 1.0, 2.5, and 3.5 km at the top of the layers G2, G3, G4 and M1 (Moho), respectively. Furthermore, to minimize computation cost, picks for crustal phases were decimated to reduce the total number of arrivals taken into account to 50,000. For MZ2 a similar number of models were generated but with maximum velocity variation at each node of ±0.5 km/s and maximum depth variation of 1, 2, 3, and 4 km for layers G2, G3, G4 and M1, respectively. The Metropolis algorithm and adaptive variance is utilized to increase the convergence: during the first half of the exploration, a pyramidal scheme that increases in 10 steps the allowed depth and velocity variation from 20 to 100% of their maximum is implemented, in order to finely explore the model space near our final model. During the second half, the maximum variations are only limited by the adaptive variance that targets an acceptance ratio of 23%.

MZ1 final model explains the traveltime and phase of 47,143 of the 49,337 events or 96% of total picks, with a RMS travel-time residual of 0.078 s. Furthermore, Loureiro et al. (2016) defined an additional parameter ranging between 0 and 1, the model score, that is able to report on the quality of a model through its ability to predict the observations while maintaining good statistical fit. The first quality thresholds used to establish the model ensemble (ME) was set to 75% of the final model's quality of fit (75% of the model score), together with thresholds of 80% explained picks, chi-squared lower or equal to 2.0 and RMS lower or equal to 0.095 s. Since the quality score is constructed taking the log of the chi-squared, our events individual (data driven) uncertainty was multiplied by 1.45 in order to obtain a final chi-squared close to 1. These results in a normalized chi-squared of our preferred model of 1.063, ensuring that all random model's scores are based on chi-squared larger than 1. We finally obtained a score of 0.954 for our final model.

MZ2 final model explains the travel-time and phase of 41,277 events or 96% of total picks, with a normalized chi-squared of 0.43 and an RMS travel-time residual of 62 ms. Here uncertainty was double, resulting in a normalized chi-squared of preferred model of 1.175, ensuring that all random model's scores are based on chi-squared larger than 1. The first quality threshold used to establish the model ensemble (ME) is set to 75% of the final model's quality of fit, together with thresholds of 80% explained picks, 175% of the chi-squared (2.174) and 118% of the RMS (95 ms) of our final model.

For MZ1 on the 50,000 generated random models during the simulation, 46,944 models were valid (i. e. the ME), and 355 met the quality thresholds. These 355 random models were then used to build the global uncertainty map presented in Figs. 14C and D.

Global uncertainty maps were then generated from the 355 and 49 random models that meet predefined thresholds for MZ1 and MZ2 respectively (Figs. 14A and B). Positive and negative velocity uncertainties are generally lower than ±0.25 km/s for both profile, except in the vicinity of the Moho where contrasts are stronger. On MZ1 there is an artifact due to the presence of a pinch-out in the Moho between 350 and 470 km model-distance. On MZ2 uncertainty reaches +0.67/−0.81 km/s: exploring ±4 km depth variations and given large velocity contrast between lower crust and upper mantle, together with the pinch out of the G4 layer at 190 km model distance, result in large velocity variations at the Moho.

Finally, vertical slices through the 50,000 random models are taken at selected locations for each profile (Fig. 15A and B): each 1D velocity profile is plotted, color-coded according to its normalized average score. Four horizontal constant depth (10, 20, 30, 40 km) and 4 to 5 vertical constant velocities (6.3, 6.5, 6.9, 7.3, 7.9 km/s) profiles are plotted together with their respective 95% confidence bounds. Our final models (in black line on panels c in Fig. 15A-B) generally follow the orange to red valley formed by the best normalized score values, attesting of the good quality of our solution. The width of the 95% confidence velocity bound rarely exceeds +/− 50 m/s. The depth bound for the lowest constant velocity profiles (6.3–6.5 km/s) is very narrow (generally less than +/− 500 m although it reaches 750 m at 250 km model distance on MZ2) as the velocity gradient in the upper crust G1 is higher than in the middle and lower crust. Hence, except where the crust begins to be thinner to the East, the depth bounds are larger as the velocity gradient in the middle crust is lower than in the upper crust. This is the case for 6.8 km/s (±0.65 to ±1.65 km) and 7.0 km/s (±0.85 to ±3.15 km onshore) on MZ1 and for 6.9 km/s on MZ2 where the depth bound is in the +/− 0.5 to +/− 2.0 km range, but reaches +/− 4.5 km at 55 km model distance. In the latter model, a velocity of 7.3 km/s is reached only in the G4 layer between 0 and 190 km distance, and the depth bound in this area is in the +/− 0.5 to +/− 1.5 km range. On MZ1, except at 250 km model offset, where it is limited due to the presence of a velocity jump around this value, the classic tendency is followed for the velocity 7.3 km/s (±0.35 to ±1 km) at the locations where our preferred model reaches higher velocities in the lower crust because of similar low gradients. To the East, approaching the MFZ and the MB, the depth bounds are much lower for the crustal layer G2, and the increase of the velocity gradient in the upper part of the crust is clearly evidenced

Table 2
: Summarizes reflected or refracted phase name, number of explained events, residual mean-square, and normalized chi-squared value for MZ2 profile.

Instrument	Position (km)	Direction	Npts	Trms (s)	Chi-squared
MZ1LSS01	−91.192	1	3172	0.075	0.283
MZ1LSS02	−89.583	1	3119	0.092	0.483
MZ1LSS03	−86.339	1	3477	0.075	0.445
MZ1LSS04	−82.262	1	3764	0.069	0.445
MZ1LSS05	−78.129	1	2940	0.066	0.368
MZ1LSS07	−71.426	1	3139	0.064	0.477
MZ1LSS08	−67.618	1	3406	0.111	1.242
MZ1LSS12	−52.279	1	2715	0.093	0.794
MZ1LSS13	−48.576	1	2845	0.086	0.926
MZ1LSS14	−45.486	1	3800	0.080	0.441
MZ1LSS15	−39.944	1	3547	0.113	1.216
MZ1LSS17	−32.914	1	3771	0.096	0.630
MZ1LSS18	−29.375	1	1709	0.055	0.177
MZ1LSS19	−25.999	1	2765	0.101	1.084
MZ1LSS20	−23.189	1	3169	0.129	1.955
MZ1LSS21	−17.756	1	1538	0.090	0.642
MZ1OBS38	0.000	1	2511	0.101	0.231
MZ1OBS38	0.000	−1	69	0.057	1.092
MZ1OBS37	12.489	1	1589	0.048	0.243
MZ1OBS37	12.489	−1	335	0.066	1.151
MZ1OBS36	25.041	1	1945	0.051	0.137
MZ1OBS36	25.041	−1	573	0.054	0.427
MZ1OBS35	37.491	1	1374	0.040	0.085
MZ1OBS35	37.491	−1	664	0.041	0.239
MZ1OBS34	49.876	1	1991	0.051	0.262
MZ1OBS34	49.876	−1	943	0.039	0.356
MZ1OBS33	62.335	1	2490	0.085	0.576
MZ1OBS33	62.335	−1	922	0.048	0.519
MZ1OBS32	74.704	1	1829	0.070	0.499
MZ1OBS32	74.704	−1	1177	0.042	0.732
MZ1OBS31	87.195	1	1428	0.067	0.549
MZ1OBS31	87.195	−1	1088	0.049	0.450
MZ1OBS30	99.800	1	1701	0.051	0.281
MZ1OBS30	99.800	−1	682	0.042	0.428
MZ1OBS29	111.328	1	1419	0.077	0.683
MZ1OBS29	111.328	−1	1456	0.051	0.321
MZ1OBS28	122.813	1	1628	0.073	0.459
MZ1OBS28	122.813	−1	1332	0.073	0.505
MZ1OBS27	134.255	1	1642	0.057	0.396
MZ1OBS27	134.255	−1	1093	0.053	0.337
MZ1OBS26	145.741	1	1843	0.074	0.418
MZ1OBS26	145.741	−1	1345	0.055	0.425
MZ1OBS25	157.124	1	1203	0.061	0.505
MZ1OBS25	157.124	−1	299	0.081	1.367
MZ1OBS24	168.574	1	1754	0.132	0.682
MZ1OBS24	168.574	−1	1232	0.056	0.359
MZ1OBS23	180.124	1	1479	0.112	0.893
MZ1OBS23	180.124	−1	1045	0.106	1.041
MZ1OBS22	191.493	1	1570	0.091	0.688
MZ1OBS22	191.493	−1	1119	0.063	0.474
MZ1OBS21	204.065	1	1559	0.072	0.379
MZ1OBS21	204.065	−1	1672	0.052	0.336
MZ1OBS20	216.642	1	1370	0.055	0.468
MZ1OBS20	216.642	−1	1279	0.050	0.378
MZ1OBS19	229.136	1	1328	0.050	0.434
MZ1OBS19	229.136	−1	2247	0.073	0.628
MZ1OBS18	241.655	1	1259	0.056	0.432
MZ1OBS18	241.655	−1	1830	0.084	1.084
MZ1OBS17	254.214	1	1576	0.049	0.287
MZ1OBS17	254.214	−1	1149	0.050	0.278
MZ1OBS16	266.598	1	1254	0.047	0.408
MZ1OBS16	266.598	−1	2452	0.072	0.597
MZ1OBS15	279.297	1	1566	0.075	0.449
MZ1OBS15	279.297	−1	1958	0.061	0.369
MZ1OBS14	291.843	1	1342	0.059	0.389
MZ1OBS14	291.843	−1	1707	0.074	0.688
MZ1OBS13	304.383	1	1127	0.057	0.508
MZ1OBS13	304.383	−1	852	0.046	0.622
MZ1OBS12	316.908	1	1577	0.049	0.308
MZ1OBS12	316.908	−1	1929	0.059	0.368
MZ1OBS11	329.462	1	1017	0.046	0.388
MZ1OBS11	329.462	−1	1030	0.071	0.603
MZ1OBS10	341.993	1	1099	0.053	0.665
MZ1OBS10	341.993	−1	1752	0.107	0.906

(*continued on next page*)

Table 2 (*continued*)

Instrument	Position (km)	Direction	Npts	Trms (s)	Chi-squared
MZ1OBS09	354.547	1	570	0.035	0.360
MZ1OBS09	354.547	−1	1182	0.051	0.348
MZ1OBS08	367.051	1	1398	0.092	0.611
MZ1OBS08	367.051	−1	1472	0.044	0.225
MZ1OBS07	379.548	1	1406	0.043	0.317
MZ1OBS07	379.548	−1	2247	0.058	0.573
MZ1OBS06	392.069	1	1388	0.051	0.795
MZ1OBS06	392.069	−1	2237	0.082	0.615
MZ1OBS05	404.587	1	1057	0.074	2.122
MZ1OBS05	404.587	−1	1802	0.066	0.500
MZ1OBS04	417.055	1	1014	0.043	0.751
MZ1OBS04	417.055	−1	932	0.140	8.767
MZ1OBS03	429.611	1	593	0.056	1.618
MZ1OBS03	429.611	−1	1256	0.052	0.530
MZ1OBS02	441.976	1	605	0.041	0.799
MZ1OBS02	441.976	−1	1556	0.053	0.712
MZ1OBS01	454.568	1	531	0.034	0.492
MZ1OBS01	454.568	−1	1651	0.070	0.898

by the proximity of the light to medium blue curves at 430 km model-distance.

Regarding more specifically the crust-mantle transition, the vertical cross-sections help to evaluate the velocity found at the base of the crust, directly above velocities typically assumed to be mantellic (velocity 7.9 km/s, panels c in Fig. 15A-B). At 250 km model-distance on MZ1 for example, the cross-section QR clearly shows that a velocity 7.3 km/s is not possible at the base of the crust, while a velocity 7.6 km/s is preferred, giving the highest score on the panel b). The general increase of the velocity toward the East as well as the thinning of the crust is clearly observed and well constrained by the vertical cross-sections, which show the evolution of the position in depth of the velocity jump at the Moho, through the position of the best scores calculated for the velocity 7.9 km/s and the velocities at the base of the crust.

6. Velocity Model & N-S Structure of the South Mozambique Region

In order to characterize the P-wave seismic velocity variations along these two profiles, 1-D velocity-depth profiles were extracted from the velocity model at 10 km interval (Fig. 16). 1-D velocity-depth profiles below the seafloor allow to discuss the properties of crust and to establish the lateral segmentation.

Table 3
Summarizes the instrument name, distance along model, direction code (−1 for rays traveling westward and 1 traveling eastward), number of explained events, travel-time residual mean-square, and normalized chi-squared value, respectively for MZ1 MZ2

Phase	Index	Npts	Trms (s)	Chi-squared
Pw	1	1675	0.019	0.269
Ps1	2	187	0.013	0.124
Ps2P	3	264	0.019	0.023
Ps2	4	873	0.026	0.409
Ps3aP/Ps3bP	5	1150	0.028	0.122
Ps3a	6	64	0.022	0.264
Ps3bP	7	131	0.019	0.026
Ps3b	8	394	0.009	0.111
Psv1aP/Psv1bP	9	908	0.024	0.064
Psv1a	10	135	0.060	0.738
Psv1bP	11	222	0.033	0.338
Psv1b	12	1173	0.023	0.396
Psv2P	13	1496	0.032	0.217
Psv2	14	2733	0.042	0.610
Pg1P	15	1415	0.042	0.205
Pg1	16	4438	0.064	0.831
Pg2P	17	762	0.103	1.067
Pg2	18	8831	0.068	0.418
Pg3P	19	276	0.077	0.452
Pg3	20	2702	0.055	0.208
Pg4P/PmP	21	3359	0.092	0.680
Pn	22	1344	0.064	0.422
Pm2P	23	2305	0.070	0.485
Pn2	24	971	0.097	0.945
Pm3P	25	1988	0.090	0.814

6.1. Nature of the Crust below the NNV

The analysis of the data on the MZ1 and MZ2 profiles confirms and extends to the whole NNV the previously published results (Fig. 2) (Moulin et al., 2020; Leprêtre et al., 2020; Schnurle et al., 2023).

From the Lebombos Complex to the shoreline, between −90 and − 50 km model-distance, 1-D velocity-depth profiles along MZ1 and between −40 and − 15 km model distance, along MZ2 were not extracted as the crust is only partially illuminated (Fig. 16A and B). Nevertheless, the estimated resolution is good (generally lower than 0.7 (MZ2)) in the highlighted parts and the area seems to reveal the westward rise of the upper crustal interfaces toward the Lebombos Complex, as an important thinning of the sedimentary sequence and the presence of higher velocities close to the surface at the western extremity of the MZ1 profile.

In the CSS, the crust slightly thinned eastward from 34 to 31 km thick in a distance of ~20 km. The top of the crust gently deepens eastward to ~5.5 km depth onshore close to the coastline. The velocities range from 5.6 to 5.8 km/s at the top of the crust up to 7.3 km/s at the base (Fig. 16C). At shallower levels, the sedimentary cover rapidly thins from ~2.5–3.0 km thick in the easternmost part of the CSS to <0.1 km or even none locally at the Central Plateau located in the center portion of the CD. The limit between the CSS and the CD segments coincides relatively well with a slope break at the continental shelf. There, the lowest unit of the sedimentary sequence as the SV series deepens toward the West, and shows when visible a well-bedded but disturbed facies in the light of the PSDM. In addition, it also locates the area of intersection with the N-S regional negative gravity anomaly (Fig. 1).

In the CD, crustal velocities are generally slightly higher than in the CSS, except in the center of the area where velocities are similar (Fig. 16D). The crust has a relatively constant thickness between 26 and 28 km, but presents increasing velocities on both edges of the area. In the western portion of the CD, velocities increase to 5.8–6.1 km/s at the top of the crust, whereas the lower crust reaches 7.2–7.4 km/s top-bottom velocities. In the eastern portion of the CD, velocities are lower in the upper crust, whereas top-bottom velocities in the lower crust reach 7.4–7.6 km/s. The areas of higher crustal velocities are further illustrated by the rise of deep interfaces from both edges of the CD. At shallower levels, the CD localized all the inter-bedded high velocities volcanic events (Fig. 3), except one located just East of the junction with the LC where higher lower crustal velocities up to 7.6–7.5 km/s are also found at the base of the crust. Relatively high velocities (4.2–4.8 km/s top-bottom SV1 velocities) from the SV sequence outcrop

Table 4
summarizes the instrument name, distance along model, direction code (−1 for rays traveling westward and 1 traveling eastward), number of explained events, travel-time residual mean-square, and normalized chi-squared value, respectively for MZ2.

Instrument	Position (km)	Direction	Npts	Trms (s)	Chi-squared
MZ2LSS01	−118.563	1	1372	0.064	0.261
MZ2LSS02	−117.936	1	816	0.056	0.198
MZ2LSS03	−113.537	1	1104	0.061	0.171
MZ2LSS04	−110.392	1	894	0.060	0.165
MZ2LSS05	−106.553	1	946	0.052	0.134
MZ2LSS06	−103.198	1	636	0.054	0.167
MZ2LSS07	−98.105	1	797	0.043	0.111
MZ2LSS08	−94.635	1	1018	0.046	0.148
MZ2LSS09	−90.789	1	1221	0.064	0.268
MZ2LSS10	−87.013	1	905	0.056	0.201
MZ2LSS11	−82.867	1	1038	0.071	0.279
MZ2LSS15	−65.509	1	665	0.063	0.328
MZ2LSS16	−62.533	1	531	0.079	0.433
MZ2LSS17	−58.621	1	354	0.082	0.462
MZ2LSS18	−52.699	1	263	0.056	0.198
MZ2LSS20	−44.974	1	404	0.070	0.341
MZ2OBS01	0	1	660	0.049	0.401
MZ2OBS02	12.562	−1	230	0.030	0.225
MZ2OBS02	12.562	1	864	0.053	0.339
MZ2OBS03	25.12	−1	429	0.021	0.172
MZ2OBS03	25.12	1	523	0.028	0.219
MZ2OBS04	37.642	−1	555	0.050	0.420
MZ2OBS04	37.642	1	846	0.037	0.211
MZ2OBS05	50.192	−1	504	0.041	0.297
MZ2OBS05	50.192	1	613	0.048	0.438
MZ2OBS06	62.696	−1	525	0.049	0.455
MZ2OBS06	62.696	1	677	0.064	1.067
MZ2OBS07	74.857	−1	437	0.029	0.294
MZ2OBS07	74.857	1	562	0.075	1.381
MZ2OBS08	86.691	−1	527	0.071	0.896
MZ2OBS08	86.691	1	789	0.055	0.332
MZ2OBS09	98.501	−1	429	0.073	1.464
MZ2OBS09	98.501	1	685	0.052	0.324
MZ2OBS10	110.248	−1	614	0.054	0.463
MZ2OBS10	110.248	1	641	0.066	0.709
MZ2OBS11	121.999	−1	552	0.055	0.418
MZ2OBS11	121.999	1	961	0.054	0.318
MZ2OBS12	133.745	−1	498	0.049	0.426
MZ2OBS12	133.745	1	922	0.109	1.248
MZ2OBS13	145.544	−1	799	0.073	0.776
MZ2OBS13	145.544	1	644	0.045	0.211
MZ2OBS14	157.289	−1	507	0.037	0.176
MZ2OBS14	157.289	1	1095	0.100	0.962
MZ2OBS15	169.615	−1	666	0.057	0.281
MZ2OBS15	169.615	1	943	0.062	0.322
MZ2OBS16	182.119	−1	574	0.061	0.438
MZ2OBS16	182.119	1	724	0.073	0.745
MZ2OBS17	194.682	−1	419	0.053	0.203
MZ2OBS17	194.682	1	462	0.118	1.036
MZ2OBS18	207.245	−1	732	0.066	0.666
MZ2OBS18	207.245	1	431	0.052	0.567
MZ2OBS19	219.809	−1	594	0.071	0.490
MZ2OBS19	219.809	1	501	0.033	0.593
MZ2OBS20	232.296	−1	781	0.069	0.582
MZ2OBS20	232.296	1	575	0.029	0.235
MZ2OBS21	244.794	−1	668	0.072	0.506
MZ2OBS21	244.794	1	505	0.028	0.246
MZ2OBS22	257.295	−1	995	0.068	0.499
MZ2OBS22	257.295	1	501	0.047	0.393
MZ2OBS23	269.862	−1	818	0.054	0.284
MZ2OBS23	269.862	1	336	0.025	0.242

at the Central Plateau, and more particularly at the location of the crossing with the MZ6 profile (Schnurle et al., 2023). On both side lower velocities (between 2.9 and 4.2 km/s) are found through SV1 below the 2 locations of clear sedimentary fillings forming sub-basins, presenting steep borders and apparent delays of reflectors at least clearly in the sedimentary sequence.

The velocity crustal structure shows that about half of the whole crust presents velocities higher than 7 km/s, increasing to 7.3 to 7.6 km/s at its base. The crust reveals also low velocity gradients in the mid- to lower crust (mainly between 0.01 and 0.03 km/s/km), whereas the upper crust G1 present a higher gradient (between 0.15 and 0.25 km/s/km) (Fig. 16C-D). These high velocities suggest the presence of larger amount of intrusive material, that it is additionally highlighted through the SV layers at shallower depths. Furthermore, the importance of the magmatism in the area through the time is further illustrated by the inter-bedded high velocity volcanic sills at different levels in the stratigraphy.

Combined with the surprisingly important thickness of the crust, the

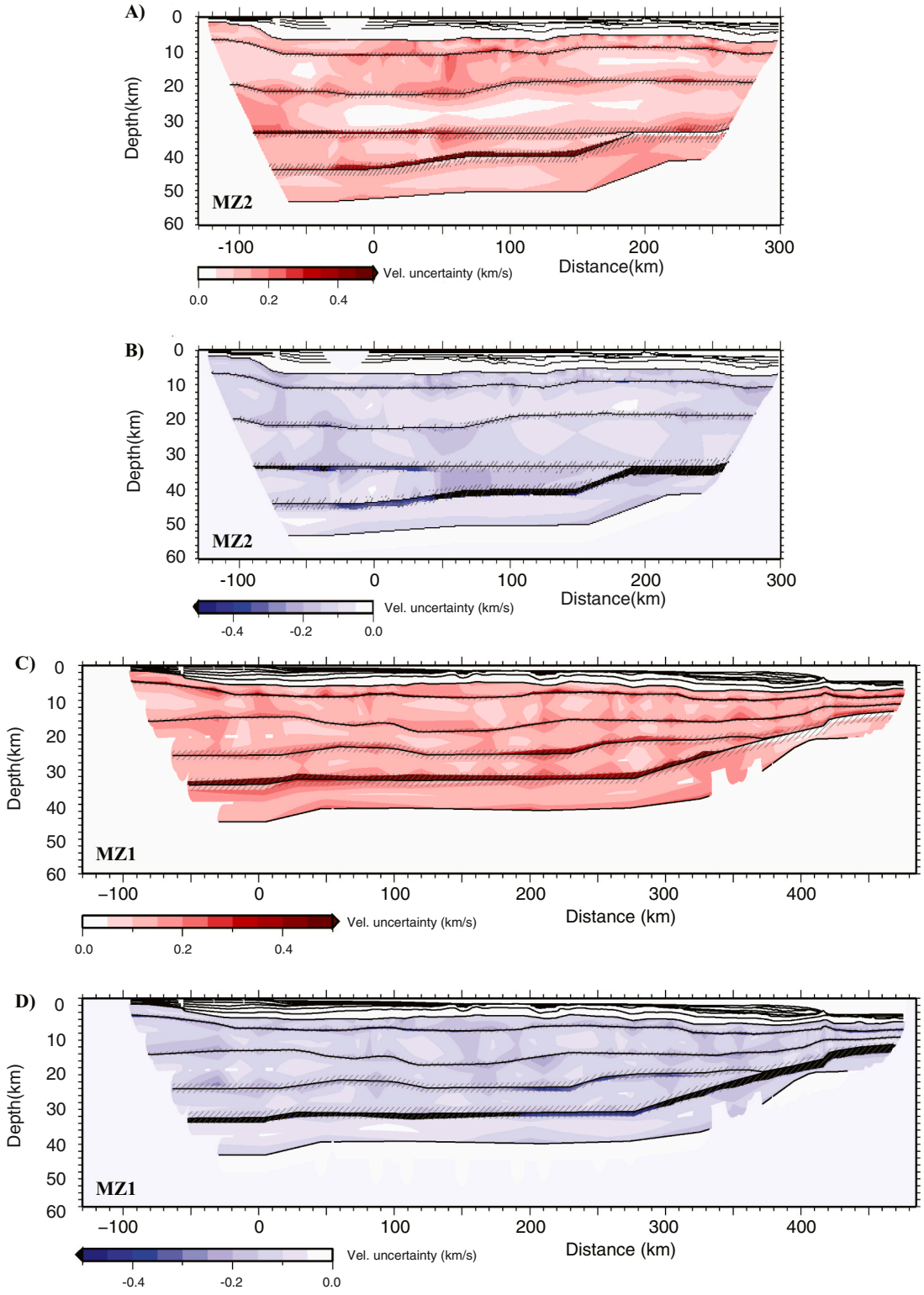

Fig. 14. : A-B: Global uncertainty map generated from the stander deviation of the 49 random models meeting our thresholds. Crust and mantel portion of our final wide-angle model MZ2. (A) Positive velocity uncertainty. (B) Negative velocity uncertainty. The hashed areas indicate the standard deviation of the depth of the interfaces explored during Vmontecarlo. Same legend in C—D for MZ1 profile, generated from the stander deviation of the 355 random models meeting our thresholds.

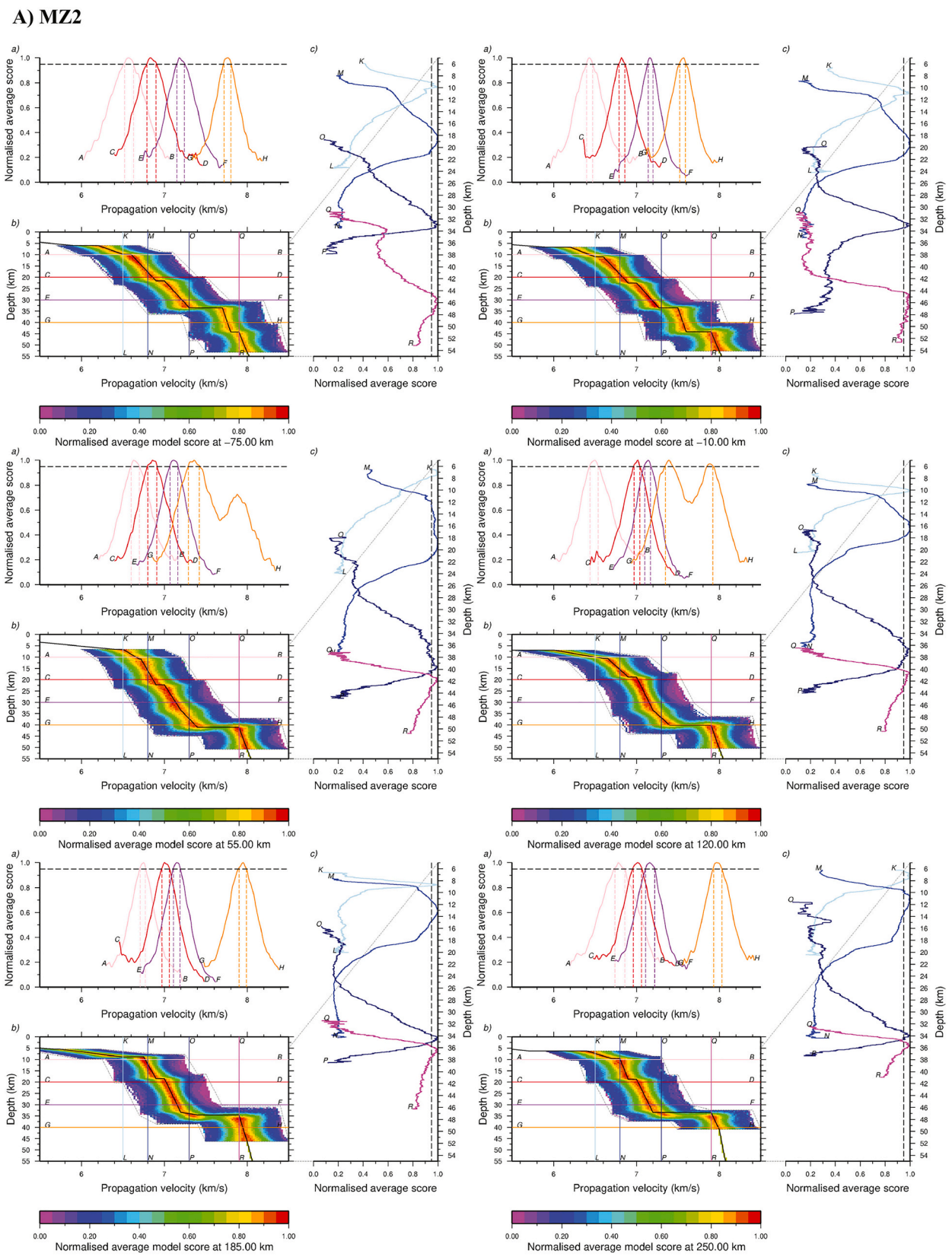

Fig. 15. : A-Evaluation of the wide-angle model MZ2 through the normalized average scores distribution at 250, 185, 120, 55, −10 and − 75 km model-distance. (b) Normalized average model scores distribution. Black line indicates the final velocity model. Thin dashed black envelope indicates the exploration domain of independent parameter uncertainties. Colored lines mark the location of horizontal (constant depth, letters A to H) and vertical (constant velocity, letters K—V) cross-sections of the average model scores presented in (a) and (c) respectively. Thick black dashlines on (a) and (c) indicate the 95% of confidence level, that is, 95% of the normalized average score. Same legend in B for MZ1 profile, through the normalized average scores distribution at 430, 350, 250, 150, 50 and − 50 km model-distance.

B) MZ1

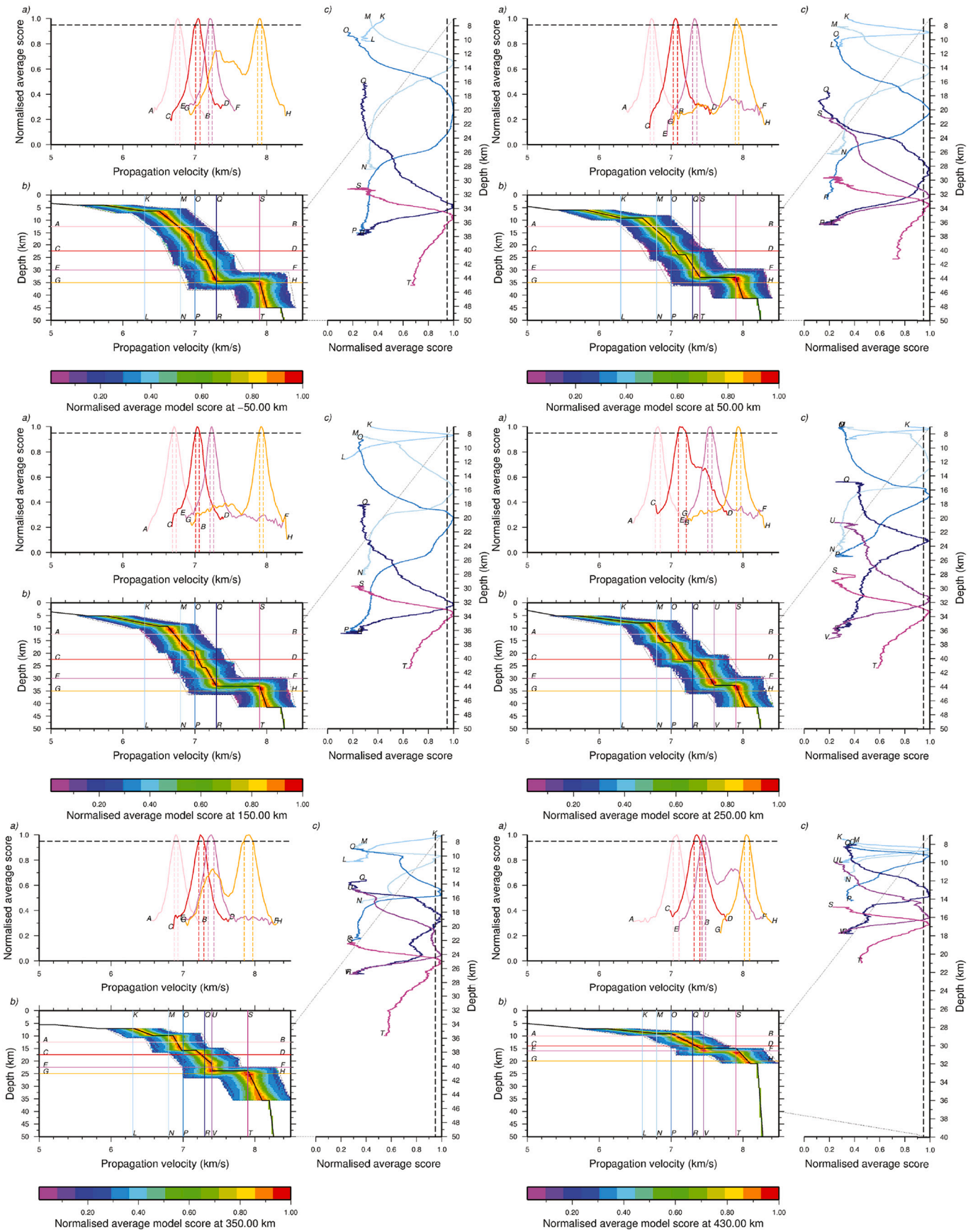

Fig. 15. (*continued*).

crustal architecture appears rather atypical in thickness and velocities, but in agreement with the other wide-angle profiles from the Moz35 experiment acquired in the NNV (*see below* the chapter in Discussion).

Along the MZ2 profile, based on the below seafloor 1-D velocity-depth profiles (Fig. 16A), we identify 3 main areas along the profile from west to east: the CSS (W-CSS and *E*-CSS), the ALR, and the LC.

Throughout the entire MZ2 model, only minor lateral velocity and gradient contrasts are observed between the G1, G2, and G3 crustal layers. At the base of the crust however, the G4 layer thins from 11 to 5 km thickness at the transition from W-CSS to E-CSS, and top-bottom velocity decreases from 7.7/7.8 to 7.2/7.6 km/s between −35 and −25 km and from 7.2/7.6 to 7.2/7.4 km/s between 30 and 50 km model distance. The Moho rises from 44 to 40 km depth between 20 and 70 km model distance (Fig. 16C). At the ALR, the crustal thickness thins to 28 km but preserves the same velocities and gradients as the CSS. In the LC, 1-D velocity-depth profiles were not extracted west of 260 km model distance as the crust is partially or not illuminated and the resolution generally lower than 0.7. Between 250 and 280 km model distance, the crustal thickness has been reduced from 32.5 to 30.5 km in order to match the relative decrease in the gravity free-air anomaly.

6.2. Nature of the Crust Below the Limpopo Corridor (LC)

Further east, the whole LC zone, observable only on MZ1, marks an area of thinned crust toward the MB from 26 km to about 12 km thick over 140 km, associated with a general increase of the crustal velocities (> 6.0 km/s) and changes in the magnetic curve character.

In more details, the LC can be separeted in two sub-segments, as proposed by Evain et al. (2021): the thinned continental crust (TCC) to the west and the corridor of anomalous crust (CAC) toward the east (Figs. 2 and 16E, red/orange and green lines respectively). By contrast with the TCC, the CAC reveals a different structural architecture regarding the crustal thickness as the organization of the sedimentary and SV sequences. In addition, in the CAC, the prominent contouritic structure coincides with a major positive free-air gravimetric anomaly (Li et al., 2021).

The lower crust G4 actually thins in a distance of ~100 km beneath the TCC and the western part of the CAC and is absent in its easternmost part. The same time, the top of the upper crust deepens through 3 steps from ~5 km depth at the CNNV to ~5.6 km depth at the TCC, and finally to ~7.5 km in average at the CAC, the main down-step occurring at the TCC / CAC limit. That is particularly well expressed with the geometry of the top of the SV sequence. Although both zones correspond to a domain of thinner crust, the TCC and the CAC differ in term of 1) total crustal thickness, 2) crustal velocities, and 3) sedimentary and SV architecture. In the TCC, velocities are relatively similar to that found just westwards in the C-NNV, with velocities of 5.7 to 6 km/s at the top of the crust and 7.3–7.5 km/s top-bottom velocities in the lower crust. Velocities increase to 6 km/s at the top of the crust arriving at the junction with the CAC domain. The crustal thickness decreases from 26 to 20 km with a major part of thinning in the lower crust G4. At shallower levels, the limit between the CD and the LC segments coincides with the end of the Central Plateau, between two ~40 km wide structural highs dawned by the SV sequence (Fig. 11). The seafloor begins to gently deepens and the sedimentary sequence to thick away from the CD toward the CAC. By contrast, the CAC only shows crustal velocities higher than 6 km/s (Fig. 16E). Indeed, aside from the crustal thinning and the rise of the Moho, velocities are higher along the TCC increasing heading east in the crustal layers G1, G2 and G3, as well as in SV2. It is particularly well pronounced for the layer G1 which has top and bottom velocities of 6.0–6.6 km/s and 6.5–6.9 km/s, progressively increasing from the limit with the TCC to the MFZ. Conversely, velocities at the base of the crust decline to 7.4 km/s but are still relatively high. The crustal thickness decreases from 20 to 12 km with a major pinch-out of the lower crust G4 in the western part of the CAC until it disappeared eastward at 370–380 km model-distance.

More broadly, all the crustal layers thins eastward along the CAC as well as the SV sequence. At shallower depths, the top of the SV sequence forms 2 relatively buried plateaus from 320 to 380 km model-distance and from 380 to 415 km model-distance, with increasing depth moving to the east before to reach the MFZ. Above, the sedimentary cover is thicker along the CAC generally >2 km, and includes a prominent contouritic domain which reaches its maximal thickness of ~3 km where the lower crustal layer G4 disappears below the junction between the 2 plateaus. That place also coincides with a steep increase in the SV velocities particularly in SV1, from top-bottom velocities of 4.0–4.9 km/s west of the junction between the 2 plateaus forming the CAC, to 5.2–5.9 km/s to the east. Note that the MZ1 MCS also presents a major change in the seismic signature through SV1 there. Then, the MFZ coincides with the limit between the CAC and the MB. It marks a small but abrupt step in the Moho topography as at the seafloor, and a relative down-step of the basement is localized just East of a major negative peak in the magnetic anomaly along MZ1.

In the MB, the top of the basement is clearly imaged on the MZ1 MCS by a strong reflector drawing a rough topography (marked by the top of the SV sequence there Fig. 11). It lies at 5.2 to 5.7 km depth, showing a small down-step at the eastern extremity of the MCS profile. Interpreting the top of the SV sequence as the top of the crust, the crustal thickness reaches a minimum there from 10 down to 8 km, with a Moho located at about 14 km depth. The velocities at the top of the crust of more or less 5 km/s reveal a significant decrease compared to what is found at the LC (Fig. 16F), while the velocities at the base of the crust of 7.40–7.45 km/s remain relatively unchanged.

7. Discussion

Due to the lack of deep seismic data, the crustal nature of the MCP and the NNV was largely controversial and speculative, although it is crucial in the understanding of the early stages of the Gondwana break-up in plate reconstructions and in the determination of the location of continent-ocean boundary (COB) in SE Africa (see *Introduction* chapter). The present study completes the discussion on the N-S South Mozambique crustal segmentation, the crustal nature of each segment, and the position of the COB. For that purpose, velocity-depth profiles were extracted every 10 km along MZ1 and M2 profiles (Fig. 16), and then compared to the compilations for Atlantic-type Oceanic Crust from Christeson et al. (2019) and for Continental Crust from Christensen and Mooney (1995).

7.1. Interpretation of the crustal structure

In order to discuss the nature of the crust below the NNV, the 1D velocity-depth profiles extracted from these 2 models are compared with the worldwide compilations of the continental crust from Christensen and Mooney (1995) and of the Atlantic Ocean from Christeson et al. (2019) in Fig. 16C-E. From the Lebombo Complex to the LC, the velocity-depth profiles show significant disparities with those of Atlantic oceanic crust: 1) the velocities at the top of the crust (5.5 to 6.5 km/s) are generally higher, 2) the crust largely thicker, with an average thickness of 29–30 km in the NNV; this thickness in high excess of 25 km are not compatible with oceanic LIPS (Moulin et al., 2020; Leprêtre et al., 2020) and 3) velocity gradients through the crust are globally very low. That makes the crustal structure in the NNV rather incompatible with normal or thickened oceanic crust. The 1D velocity-depth profiles appear more easily comparable with the worldwide compilation for continental crust from Christensen and Mooney (1995), showing more similar thicknesses and lower velocity gradients. However, velocities along the MZ1 model are higher than those found in the compilation, as the velocity gradient

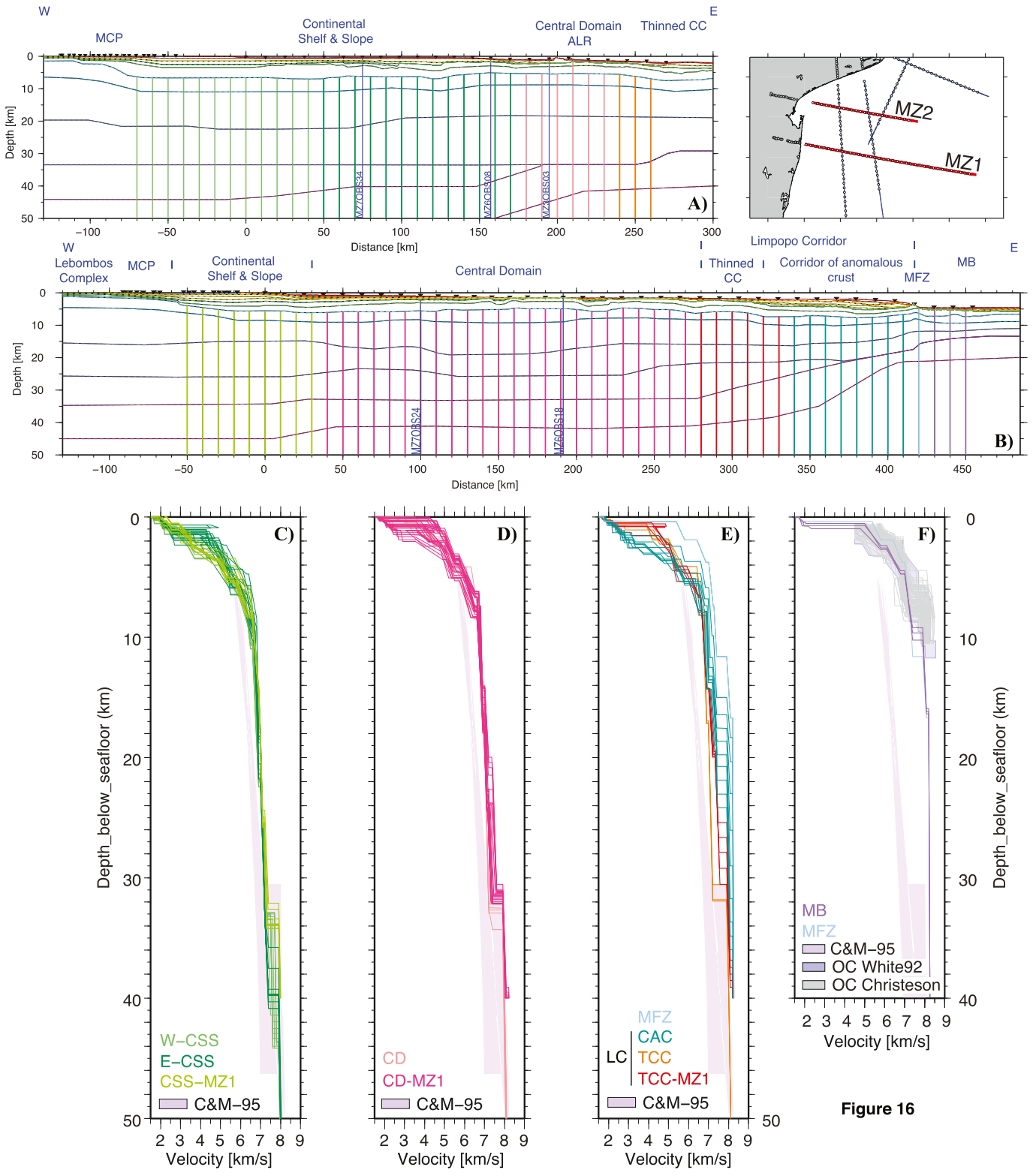

Figure 16

Fig. 16. : Insert of MOZ3/5 dataset (blue lines), MZ1 and MZ2 profiles are indicated by red lines. OBS and LSS locations are indicated by white circles. Comparison of the 1-D velocity-depth profiles (1D velocity profiles) extracted from the final P-waves velocity models for different domains along the MZ1 (b) and MZ2 (a) profiles with compilations from the literature. Distribution of the 1-D velocity-depth profiles extracted and presented in (c) - (f). The color-code is according to the segmentation along MZ1 and MZ2. (c) Comparison of the 1D velocity profiles extracted in the CSS with the compilation for Continental Crust (CC) from Christensen and Mooney, 1995. (d) Comparison of the 1D velocity profiles extracted in the CD with the compilation for Continental Crust (CC) from Christensen and Mooney, 1995. (e) Comparison of the 1D velocity profiles extracted in the LC with the compilation for Continental Crust (CC) from Christensen and Mooney, 1995 and (f) Comparison of the 1D velocity profiles extracted in the MB with the compilation for Oceanic Crust from Christeson et al., 2019. CSS, Continental Shelf & Slope; CD, Central Domain; LC, Limpopo Corridor; TCC, Thinned Continental Crust; CAC, corridor of anomalous crust; MB, Mozambique Basin; MFZ, Mozambique Fracture Zone. (For interpretation of the references to color in this figure legend, the reader is referred to the web version of this article.)

in the upper crust, particularly in the LC. Velocities observed along the MZ2 profile are however 0.5 to 1 km/s higher than observed (generally) elsewhere, most particularly at its top (Fig. 16C), but at the crossing with MZ3, MZ6, and MZ7, velocity and velocity gradients are consistent (within the uncertainty bounds – Evain et al., 2021; Leprêtre et al., 2020; Schnurle et al., 2023).

For the crustal discussion in the LC (Limpopo Corrirdor), we compared the 1D velocity-depth profiles in the MB with the Continental Crust velocity-depth bounds from Christensen and Mooney (1995) and the Oceanic Crust velocity-depth bounds of the Atlantic Ocean (Christeson et al., 2019) (Fig. 16E). Considering the top of the crust at the position of the Top-SV modeling interface, the 1D velocity-depth profiles are very close to that found for oceanic crust in term of gradient and velocities, while the crust remains slightly thicker (8–10 km) and velocities relatively high at its base (~7.4 km/s) and crustal velocity gradients lower.

Finally, in the MB, the 1-D velocity-depth profile extracted there clearly shows high velocities close to the seafloor (> 4 km/s), and globally a sharp increase of the crustal velocities (Fig. 16E-F), that suggests additional magmatism such as buried seamounts at the top of the crust.

In summary, the data of MZ1 and MZ2 profiles confirm and complete the results already published (Moulin et al., 2020; Leprêtre et al., 2020; Evain et al., 2021; Watremez et al., 2021; Schnurle et al., 2023; Babonneau et al., 2022):

1) the interpretation of the intersecting wide-angle and MCS MZ2, MZ1 and MZ6 and MZ7 profiles demonstrates a continuity of the velocity structure between MCP and NNV with a ~ 35–40 km thick crust of continental nature gently thinning under the South MCP and the CSS, to about ~30 km in the major part of the NNV. In the NNV, several intense magmatic activities (from Karoo to Miocene events) have contributed to modify the propriety of the crust (e.g., Vp > 7.2 km/s) (by intrusion, underplating, metamorphism, etc.…, overloading the NNV crust, and generated a general increase in velocities) (Moulin et al., 2020; Leprête et al., 2021). The CD seems to localized a major magmatic intrusion including high velocities up to 7.5 km/s at the base of the crust.
2) the crustal structure of the MCP and surrounding NNV shows a clear resemblance with the two conjugate cratons at the time of the Gondwana assemblage: both crustal structures estimated along the Lebombo monocline (35–38 km) (Kwadiba et al., 2003; Nguuri et al., 2001, etc) and below the Grunehogna craton in Antarctica (Hubscher et al., 1996) are similar to the one described by our results (see Moulin et al., 2020 for more details).
3) The Limpopo Corridor is an about 100 km wide N-S corridor with two segments limited by deeply rooted faults: the Limpopo fault to the west and the MFZ to the east. The westward segment evidences the thinning and temination of the MCP et NNV continental crust, while toward the east, the segment presents mixed crust interpreted as exhumed/flowed lower continental crust with magmatic intrusions. They infer that strike-slip or highly oblique rifting occurred along the LM (see Evain et al., 2021 for more details). The N—S trending positive gravity anomalies are related to the presence of contourites above this thinned intruded continental crust.

7.2. Impact on these results on our understanding of the Gondwana situation

Fig. 17 presents a compilation of a mean crustal thickness distribution in the East Gondwana, using published wide-angle results in Africa (Kwadiba et al., 2003; Nair et al., 2006; Leinweber et al., 2013; Domingues et al., 2016; Mueller et al., 2016) and in the Antarctica (Hubscher et al., 1996, modified from Kudryavtzev et al., 1991; Baranov and Morelli, 2013) together with the Pamela-MOZ3–5 wide-angle results. In order to compare the two sides of this part of Gondwana, the compilation is resituated in the tightest kinematic reconstruction of Thompson et al. (2019) as this is the only reconstruction that does not show overlap between the thick African and Antarctic continental crusts and therefore respects the Pamela-Moz3–5 wide-angle results.

On both sides, there is very thick continental crust, from 38 km to >50 km, with similar velocity structure (Moulin et al., 2020; Leprêtre et al., 2020). On the African plate, the Lebombo and Mateke-Sabi monoclines delimit an area constituted by the MCP and the NNV, with a crustal thickness slightly lower (38-42 km in the MCP and 25–39 km in the NNV; Leprêtre et al., 2020). On the Antarctica plate, the Grunehogna craton, fringed to the east by the Maud belt, presents also a crustal thickness similar to the MCP.

In the MB, the Continental-Oceanic Boundary (COB) is located close to the coast in the Angoche Basin, in the north-eastern corner and just south the Beira continental High, where the oldest magnetic anomaly identified is dated at 155–157 Ma, in Kimmeridgian time (Mueller and Jokat, 2019). In the NNV, the COB and its associated necking zone are located at the junction between the North and South Natal Valley, south to the Naude Ridge, probably at the location of the Ariel Graben, in good agreement with the proposition of Goodlad (1986). There, the oldest anomaly in this area is supposed to be M12 (Martin et al., 1981), associated with the Valanginian southwestward motion of Patagonia plate along the Agulhas-Falkland Fracture Zone. This motion together with the SSW motion of the Antarctica plate produced a Ridge-Ridge-Ridge Triple Junction generating the Mozambique ridge (Fischer et al., 2017).

In between the two plates, the N-S LC exhibits a very narrow margin with a steep necking zone at the termination of the MCP/NNV continental crust and a central corridor of anomalous crust bounded to the east by the Mozambique fracture zone and the oceanic crust of the MB, produced by ductile shearing responsible for the thinning of the continental crust and an oceanwards flow of lower crustal material (Evain et al., 2021, this study).

Consistent with the proposition of a full extent of the Pan-African orogenic event into Gondwana (Jacobs and Thomas, 2004), the Pamela-MOZ3–5 wide-angle results suggest a continuity of the Kaapval and Grunghena cratons and the MCP and NVV (Fig. 18). The Grunghena craton represents therefore on Antarctica a piece of Proto-kalahari shield, as the Sao Luis craton is a piece of the West African Shield in the equatorial Ocean (Hurley et al., 1967; Trompette, 1994; Moulin et al., 2010).

Whilst the entire East Gondwana was impacted by the Oxfordian/Kimmeridgian kinematic phase, allowing the initiation of the Somalia (Davis et al., 2016) and Mozambique (König and Jokat, 2010) oceanic basins (Thompson et al., 2019), it did not produce a complete disruption within the East African Antarctic orogeny (EAAO). In the MB, the continental Beira High (Mueller et al., 2016; Mueller and Jokat, 2017; Mueller and Jokat, 2019) behaves like a piece torn from Mozambique. Such microblocks are common in 'buffer' areas between two geodynamicly different domains (for instance, the Danakil block: Sichler, 1980; McClusky et al., 2010; the Jan Mayen microcontinent: Talwani and Eldholm, 1977; Gaina et al., 2009; the Iberian subplate: Olivet, 1996; the Santos block: Moulin et al., 2012).

Therefore, eastward of the EAAO, the Oxfordian/Kimmeridgian kinematic phase implies the initiation of oceanic crust in the two Somalia and Mozambique Basin. Westward of the EAAO, the Oxfordian/Kimmeridgian kinematic phase also impacted the MCP, the NNV, the South-African southern margins (Paton and Underhill, 2004) and the Falkland margin (Jones et al., 2019), but only producing light thinning, magmatic intrusions, subsidence and sedimentary basins, without complete break-up and oceanic basin initiation. In these areas, the oceanic spreading will only start during the Valanginian-Barremian phase, with the south-eastward motion of the Patagonia sub-plate and the opening of the South Atlantic Ocean.

8. Conclusions

The aims of Pamela MOZ35 wide-angle experiment was to answer to questions that are still matter of debate: the architecture, the nature and position of the first oceanic crust, the link with the Lebombo mountains and MCP, the ages of volcanism, the geodynamic evolution and the timing.

The processing and analysis of these new data show that

- The MCP is a 34–39 km thick continental block with velocities in the upper crust from 5.6 to 6.3 km/s and in the lower crust, up to 7.1 km/s. The MCP presents a W-shape basin, with strong reflectors, dated by Schnurle et al., 2023 to Kimmeridgian to Berriasian-Valanginian, younger than previously thought.
- The NNV is of the same continental nature, but 10 km thinner, with top-bottom velocities ranging from 5.8 to 6.1 km/s in the upper crust, to 7.2–7.6 km/s in the lower crust.
- In the CD of the NNV, the lower part of the crust exhibits velocity variations that are probably connected to mafic intrusions. The surface is impacted by volcanism (Almirante Leite Ridge) and a plateau shape, with very few sediment on the top. The ALR is SW-NE elongated structure, with the same direction than the Beira High and the Naude Ridge

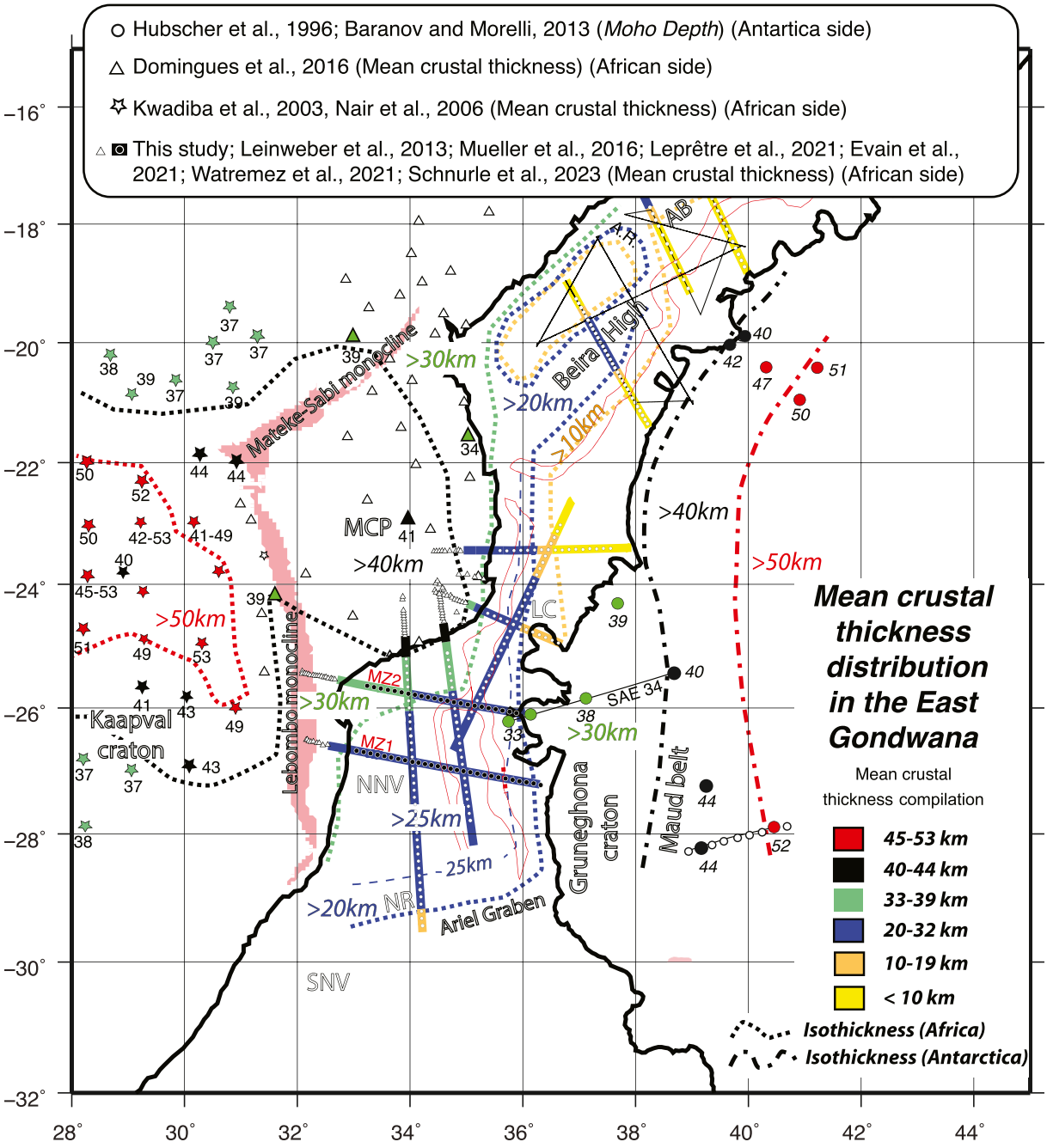

Fig. 17. : Zooming on the tightest kinematic reconstruction of Thompson et al. (2019), with a compilation of a mean crustal thickness distribution in the East Gondwana, using published wide-angle results in Africa (Kwadiba et al., 2003; Nair et al., 2006; Leinweber et al., 2013; Domingues et al., 2016; Mueller et al., 2016) and in the Antarctica (Hubscher et al., 1996, modified from Kudryavtzev et al., 1991; Baranov and Morelli, 2013) together with the Pamela-MOZ3–5 wide-angle results (Moulin et al., 2020; Leprêtre et al., 2021; Evain et al., 2021; Watremez et al., 2021; Schnurle et al., 2023; this study). AB, Angoche Basin; AG, Ariel Graben; MCP, Mozambique Coastal Plain; NNV, North Natal Valley; NR, Naude Ridge; SNV, South Natal Valley; LC, Limpopo Corridor.

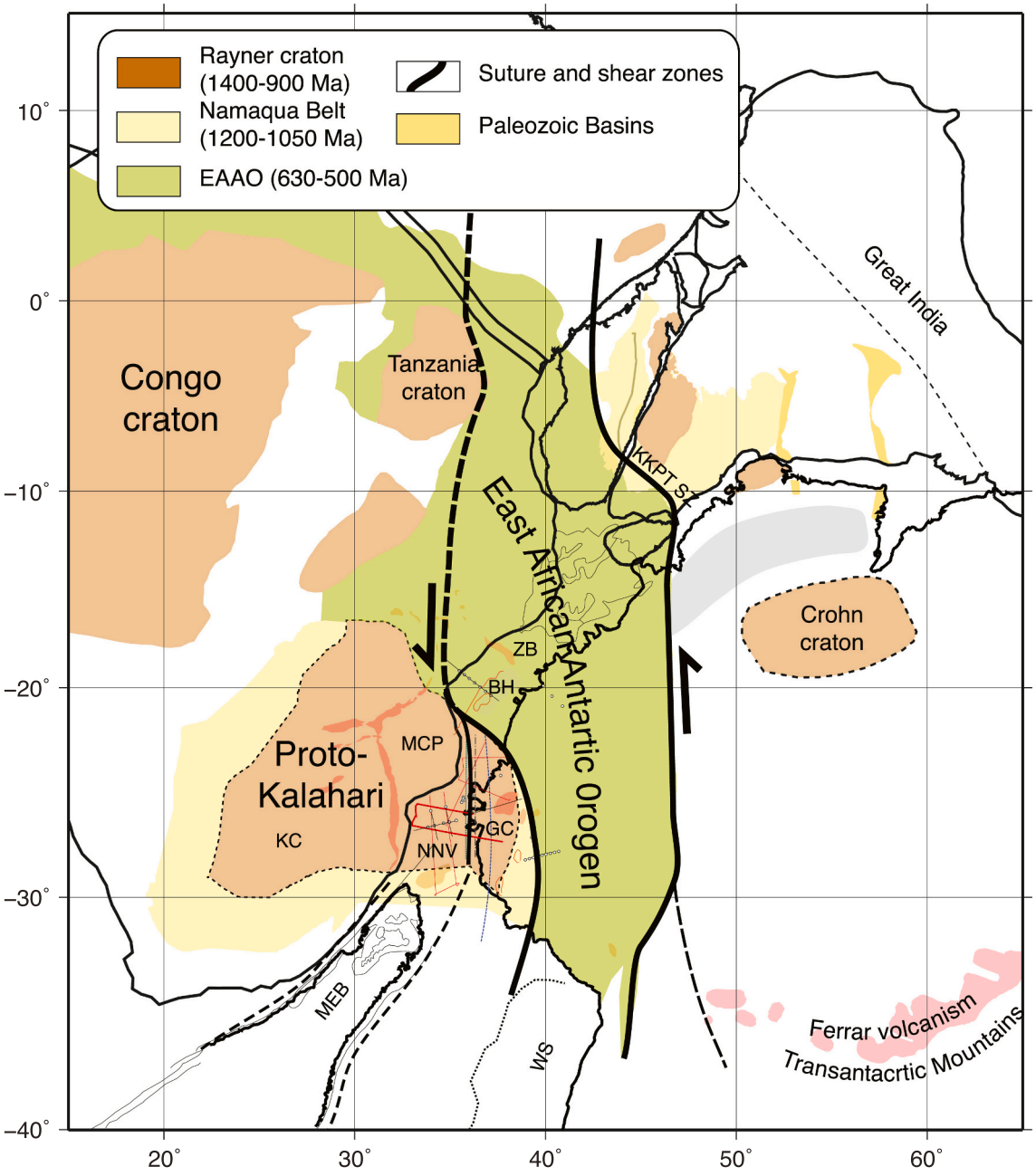

Fig. 18. : Revised geodynamic map of NNV and neighouring areas in a Gondwana reconstruction, modified from Jacobs and Thomas, 2004, on the base of Pamela-MOZ3–5 wide-angle results (Moulin et al., 2020; Leprêtre et al., 2021; Evain et al., 2021; Watremez et al., 2021; Schnurle et al., 2023; this study).

- The Naude Ridge is strictly speaking the Necking zone, followed by oceanic crust of Valanginian age (Leprêtre et al., 2020)
- To the East, the LC represents also a necking zone, with thinned continental crust. Its thickness seems to have some variation from north to south. It is fringed in the Limpopo Margin by an uplifted block and is the place of erosional processes, Mass Transport Deposits and Contourites, probably due to the conjunction of the slope produced by the uplift and the eddies (Babonneau et al., 2022).
- Our reconstruction and results coincide with the expectations of the geologists of the pan-African East Gondwana, with a good and coherente assemblage of the different tectonics blocks (like the two late Mesopro- terozoic/Early Neoproterozoic mobile belts meet, and also the 600–500 Ma East African–Antarctic Orogen), suture and shear zones.

CRediT authorship contribution statement

M. Moulin: Conceptualization, Investigation, Methodology, Project administration, Supervision, Visualization, Writing – original draft, Writing – review & editing. **A. Leprêtre:** Formal analysis, Methodology, Visualization, Writing – original draft. **F. Verrier:** Formal analysis. **P. Schnurle:** Formal analysis, Methodology, Supervision, Visualization, Writing – review & editing. **M. Evain:** Formal analysis, Investigation, Methodology, Project administration, Supervision, Visualization, Writing – review & editing. **P. de Clarens:** Methodology, Visualization. **J. Thompson:** Methodology, Visualization. **A. Afilhado:** Investigation. **A. Loureiro:** Investigation. **D. Aslanian:** Conceptualization, Investigation, Methodology, Project administration, Supervision, Visualization, Writing – original draft, Writing – review & editing.

Financial support

This research has been supported by the PAMELA (PAssive Margins Exploration Laboratories) project funded by TOTAL (grant agreement no FR000008206) and Institut Français de Recherche pour l'Exploitation de la Mer (grant agreement no 15/1212133/BF).

Declaration of Competing Interest

The authors declare that they have no known competing financial interests or personal relationships that could have appeared to influence the work reported in this paper.

Data availability

The authors do not have permission to share data.

Acknowledgements

We thank the captain, crew, and MCS technical team of the R/V Pourquoi-Pas. We also thank the OBS technical team who maintain and constantly improve our OBS pool, as well as the land stations deployment team. The PAMELA (PAssive Margins Exploration Laboratories) project was initiated in the early 2010th by TOTAL and IFREMER in collaboration with French universities (Université de Bretagne Occidentale, Université Rennes 1, Université Pierre and Marie Curie), the CNRS and the IFPEN. A Leprêtre and F. Verrier respective post-doc studies and contract were co-funded by TOTAL and Ifremer as part of the PAMELA scientific project. The GMT (Wessel and Smith, 1998), Seismic Unix (Cohen and Stockwell, 2019; Stockwell, 1999), and Geocluster (CGG-Veritas) software packages were used extensively in this study. We thank the Editor, Ramon Carbonell, the reviewer Anouk Beniest and one other anonymous reviewer for their comments, which substantially improved the manuscript.

References

Aslanian, D., Moulin, M., Evain, M., Schnurle, P., 2021. Comment on 'The challenge in restoring magma-rich rifted margins: the example of the Mozambique-Antarctica conjugate margins' by Tomasi S., Kusznir N., Manatschal G. & Despinois F. Gondwana Res. 103, 401–403. https://doi.org/10.1016/j.gr.2021.10.019.

Auffret, Y., Pelleau, P., Klingelhoefer, F., Géli, L., Crozon, J., Lin, J.I., Sibuet, J.-C., 2004. MicrOBS : a new generation of bottom seismometer. First Break 22, 41–47.

Babonneau, N., Raisson, F., Genêt, A., Lopes, U., Fierens, R., Miramontes, E., Révillon, S., Rabineau, M., Droz, L., Belleney, D., Aslanian, D., Moulin, M., 2022. Contourite on the Limpopo Corridor, Mozambique margin: long-term evolution, facies distribution and Quaternary processes. Sedimentology 70 (3), 728–758. https://doi.org/10.1111/sed.13045.

Baranov, A., Morelli, A., 2013. The Moho depth map of the Antarctica region. Tectonophysics 609, 299–313.

Christensen, N. I. and Mooney, W. D., 1995. Seismic velocity structure and composition of the continental crust: a global view, J. Geophys. Res.-Sol. Ea., 100, 9761–9788, doi: https://doi.org/10.1029/95JB00259, 1995.

Christeson, G.L., Goff, J.A., Reece, R.S., 2019. Synthesis of oceanic crustal structure from two-dimensional seismic profiles. Rev. Geophys. 57, 504–529. https://doi.org/10.1029/2019RG000641.

Cohen, J., Stockwell, J.J.W., 2019. CWP/SU: Seismic UnxRelease no. 44: an open source software package for seismic research and processing.

Davis, J.K., Lawver, L.A., Norton, I.O., Gahagan, L.M., 2016. New Somali Basin magnetic anomalies and a plate model for the early Indian Ocean. Gondwana Res. 34, 16–28.

Dingle, R.V., Scrutton, R.A., 1974. Continental breakup and the development of post-Paleozoic sedimentary basins around southern Africa. The Geological Society of America Bulletin 85, 1467–1474.

Domingues, A., Silveira, G., Ferreira, A.M., Chang, S.-J., Custódio,, S., and Fonseca, J. F., 2016. Ambient noise tomography of the East African Rift in Mozambique. Geophys. J. Int. 204 (1565–1578), 2016. https://doi.org/10.1093/gji/ggv538.

Eagles, G., König, M., 2008. A model of plate kinematics in Gondwana breakup. Geophys. J. Int. 173, 703–717.

Evain, M., Schnürle, P., Leprêtre, A., Verrier, F., Watremez, L., Dias, N.A., Afilhado, A., Loureiro, A., Corela, C., de Clarens, P., Aslanian, D., Moulin, M., 2021. Crustal structure of the East-African Limpopo margin, a strike-slip rifted corridor along the continental Mozambique Coastal Plain and North-Natal Valley. Solid Earth 12, 1865–1897. https://doi.org/10.5194/se-2020-209.

Fischer, M.D., Uenzelmann-Neben, G., Jacques, G., Werner, R., 2017. The Mozambique Ridge: a document of massive multistage magmatism. Geophys. J. Int. 208, 449–467.

Gaina, C., Gernigon, L., Ball, P., 2009. Palaeocene–Recent plate boundaries in the NE Atlantic and the formation of the Jan Mayen microcontinent. J. Geol. Soc. Lond. 166, 601–616. https://doi.org/10.1144/0016-76492008-112.

Gaina, C., Torsvik, T., Van Hinsbergen, D., Medvedev, S., Werner, S., Labails, C., 2013. The African Plate: a history of oceanic crust accretion and subduction since the Jurassic. Tectonophysics. https://doi.org/10.1016/j.tecto.2013.05.037.

Goodlad, S.W.. Tectonic and sedimentary history of the Mid-Natal Valley (S.W. Indian Ocean). available at: http://hdl.handle.net/11427/23640.

Goodlad, S.W., Martin, A.K., Hartnady, C.J.H., 1982. Mesozoic magnetic anomalies in the southern Natal Valley. Nature 295, 686–688. https://doi.org/10.1038/295686a0.

Green, A.G., 1972. Seafloor spreading in the Mozambique Channel. Nat. Phys. Sci. 236, 19–21. https://doi.org/10.1038/physci236019a0.

Hanyu, T., Nogi, Y., Fujii, M., 2017. Crustal formation and evolution processes in the Natal Valley and Mozambique Ridge, off South Africa. Polar Science 13, 66–81. https://doi.org/10.1016/j.polar.2017.06.002.

Hubscher, C., Jokat, W., Miller, H., 1996. Crustal structure of the Antarctic continental margin in the Eastern Weddell Sea. In: Storey, B.C., King, E.C., Livermore, R.A. (Eds.), Weddell Sea Tectonics and Gondwana Break-Up, 108. Geological Society Special Publication, London, UK, pp. 165–174.

Hurley, P.M., de Almeida, F.F.M., Melcher, G.C., Cordani, U.G., Rand, J.R., Kawashita, K., Vandoros, P., Pinson, W.H., Fairbairn Jr., H.W., 1967. Test of continental drift by comparison of radiometric ages. A pré-drift reconstruction shows matching geologic age provinces in West Africa and Northern Brazil. Science 157, 495–500.

Jacobs, J., Thomas, R.J., 2004. Himalayan-type indenter-escape tectonics model for the southern part of late Neoproterozoic-early Paleozoic East African-Antarctic orogen. Geology 32, 721–724. https://doi.org/10.1130/G20516.1.

Jones, D., McCarthy, D.J., Dodd, T.J.H., 2019. Tectonostratigraphy and the petroleum systems in the Northern sector of the North Falkland Basin, South Atlantic. Mar. Pet. Geol. 103, 150–162.

Klausen, M.B., 2009. The Lebombo monocline and associated feeder dyke swarm; diagnostic of a successful and highly volcanic rifted margin? Tectonophysics 268, 42–62.

König, M., Jokat, W., 2006. The Mesozoic breakup of the Weddell Sea. J. Geophys. Res. 111, B12102. https://doi.org/10.1029/2005JB004035.

König, M., Jokat, W., 2010. Advanced insights into magmatism and volcanism of the Mozambique Ridge and Mozambique Basin in the view of new potentialfield data. Geophys. J. Int. 180 (1), 158–180.

Kudryavtzev, G.A., Butzenko, V.V., Kadmina, I.N., 1991. Crustal section across the western Dronning Maud Land continental margin from geophysical data. In: Abstracts, Sixth International Sysmposium on Antarctic Earth Sciences. National Institute for Polar Research, Tokyo, pp. 330–335.

Kwadiba, M.T.O.G., Wright, C., Kgaswanea, E.M., Simon, R.E., Nguuri, T.K., 2003. Pn arrivals and lateral variations of Moho geometry beneath the Kaapvaal craton. Lithos 71, 393–411. https://doi.org/10.1016/j.lithos.2003.07.008.

Lafourcade, P., 1984. *Etude géologique et géophysique de la marge con- tinentale du sud Mozambique (17°S à 28°S)*. Thesis. Université Pierre et Marie Curie, Paris VI, France.

Leinweber, V., Jokat, W., 2011. Is there continental crust underneath the northern Natal Valley and the Mozambique Coastal Plains? Geophys. Res. Lett. 38, 87–101. https://doi.org/10.1029/2011gl047659.

Leinweber, V., Klingelhoefer, F., Neben, S., Reichert, C., Aslanian, D., Matias, L., Jokat, W., 2013. The crustal structure of the Central Mozambique continental margin—wide-angle seismic, gravity and magnetic study in the Mozambique Channel, Eastern Africa. Tectonophysics 599, 170–196. https://doi.org/10.1016/j.tecto.2013.04.015.

Leprêtre, A., Schnürle, P., Evain, M., Verrier, F., Moorcroft, D., de Clarens, P., Dias, N., Afilhado, A., Loureiro, A., Leroy, S., d'Acremont, E., Aslanian, D., Moulin, M., 2020. Deep structure of the North Natal Valley, from the Mozambique Coastal Plain to the Naude Ridge, using combined wide-angle and reflection seismic data. J. Geophys. Res. https://doi.org/10.1029/2020JB021171.

Li, H., Tang, Y., Moulin, M., Aslanian, D., Evain, M., Schnürle, P., Leprêtre, A., Li, J., 2021. Seismic evidence for crustal architecture and stratigraphy of the Limpopo Corridor: New insights into the evolution of the sheared margin offshore southern Mozambique. Mar. Geol. 435 (106468), 2021. https://doi.org/10.1016/j.margeo.2021.106468.

Loureiro, A., Afilhado, A., Matias, L., Moulin, M., Aslanian, D., 2016. Monte Carlo approach to assess the uncertainty of wide-angle layered models: Application to the Santos Basin, Brazil. Tectonophysics 683, 286–307. https://doi.org/10.1016/j.tecto.2016.05.040.

Ludwig, W.J., Nafe, J.E., Simpson, E.S.W., Sacks, S., 1968. Seismic-refraction measurements on the Southeast African Continental margin. J. Geophys. Res. 73, 3707–3719. https://doi.org/10.1029/JB073i012p03707.

Lutter, W.J., Nowack, R.L., 1990. Inversion for crustal structure using reflections of the PASSCAL Ouachita experiment. Geophys. J. Int. 95, 4633–4646.

Martin, A.K., Hartnady, C.J.H., Goodlad, S.W., 1981. A revised fit of South America and South Central Africa. Earth Planet. Sci. Lett. 54, 295–305. https://doi.org/10.1016/0012-821X(81)90012-1.

McClusky, S., Reilinger, R., et al., 2010. Kinematics of the southern Red Sea–Afar Triple Junction and implications for plate dynamics. Geophys. Res. Lett. 37, L05301. https://doi.org/10.1029/2009GL041127.

Moulin, M. and Aslanian, D., 2016. PAMELA-MOZ03 cruise, RV Pourquoi pas?, doi: 10.17600/16001600, 2016.

Moulin, M., Evain, M., 2016. PAMELA-MOZ05 cruise. https://doi.org/10.17600/16009500.

Moulin, M., Aslanian, D., Unternehr, P., 2010. A new starting point for the history of the Equatorial and South Atlantic. Earth Sci. Rev. 98, 1–37.

Moulin, M., Aslanian, D., Rabineau, M., Patriat, M., Matias, L., 2012. Kinematic keys of the Santos – Namibe basins. In: Mohriak, W.U., Danforth, A., Post, P.J., Brown, D.E., Tari, G.C., Nemcok, M., Sinha, S.T. (Eds.), Conjugate Divergent Margins. London, Geological Society. https://doi.org/10.1144/SP369.3. Special Publications.

Moulin, M., Aslanian, D., Evain, M., Leprêtre, A., Schnurle, P., Verrier, F., Thompson, J., Clarens, P.D., Leroy, S., Dias, N., 2020. Gondwana breakup: Messages from the North Natal Valley. Terra Nova 32, 205–214. https://doi.org/10.1111/ter.12448.

Mueller, C.O., Jokat, W., 2017. Geophysical evidence for the crustal variation and distribution of magmatism along the central coast of Mozambique. Tectonophysics. 712–713, 684–703. https://doi.org/10.1016/j.tecto.2017.06.007.

Mueller, C., Jokat, W., 2019. The initial Gondwana break-up: a synthesis based on new potential field data of the Africa-Antarctica Corridor. Tectonophysics 750, 301–328.

Mueller, C.O., Jokat, W., Schreckenberger, B., 2016. The crustal structure of Beira High, Central Mozambique—combined investigation of wide-angle seismic and potential field data. Tectonophysics 683, 233–254.

Nair, S.K., Gao, S.S., Liu, K.H., Silver, P.G., 2006. Southern African crustal evolution and composition: Constraints from receiver function studies. Journal of Geophysical Research: Solid Earth 111, B02304. https://doi.org/10.1029/2005jb003802.

Nguuri, T.K., Gore, J., James, D.E., Webb, S.J., Wright, C., Zengeni, T.G., Kaapvaal Seismic Group, 2001. Crustal structure beneath southern Africa and its implications for the formation and evolution of the Kaapvaal and Zimbabwe cratons. Geophys. Res. Lett. 28, 2501–2504. https://doi.org/10.1029/2000gl012587.

Nguyen, L.C., Hall, S.A., Bird, D.E., Ball, P.J., 2016. Reconstruction of the East Africa and Antarctica continental margins. J. Geophys. Res. *Solid Earth* 121, 4156–4179. https://doi.org/10.1002/2015JB012776.

Olivet, J.-L., 1996. Kinematics of the Iberian Plate. Bulletin des Centres de Recherches Exploration–Production Elf Aquitaine 20, 131–195.

Paton, D., Underhill, J., 2004. Role of crustal anisotropy inmodifying the structural and sedimentological evolution of extensional basins: the Gamtoos Basin, South Africa. Basin Research 16, 339–359. https://doi.org/10.1111/j.1365-2117.2004.00237.x.

Powell, C., Johnson, B.D., Veevers, J.J., 1980. A revised fit of east and west Gondwanaland. Tectonophysics 63, 13–29.

Roche, V., Leroy, S., Guillocheau, F., Revillon, S., Rufet, G., Watremez, L., et al., 2021. The Limpopo magma-rich transform margin (South Mozambique) – part 2: Implications for the Gondwana breakup. Tectonics. https://doi.org/10.1029/2021TC006914.

Ryan, W.B.F., Carbotte, S.M., Coplan, J.O., O'Hara, S., Melkonian, A., Arko, R., et al., 2009. Global Multi-Resolution Topography synthesis, *Geochemistry, Geophysics*. Geosystems 10, Q03014. https://doi.org/10.1029/2008GC002332.

Salman, G., Abdulla, I., 1995. Development of the Mozambique and Ruvuma sedimentary basins, offshore Mozambique. Sediment. Geol. 96, 7–41. https://doi.org/10.1016/0037-0738.

Sandwell, D.T., Smith, W.H.F., 2009. Global marine gravity from retracked Geosat and ERS-1 altimetry: Ridge segmentation versus spreading rate. J. Geophys. Res. 114 (B1), B01411. https://doi.org/10.1029/2008JB006008.

Schneider, W.A., Backus, M., 1964. Ocean-bottom seismic measurements off the California coast. J. Geophys. Res. 69 (6), 1135–1143.

Schnurle, P., Leprêtre, A., Evain, M., De Clarens, P., Thompson, J., Dias, N., Afilhado, A., Loureiro, A., Leroy, S., d'Acremont, E., Aslanian, D., Moulin, M., 2023. Crustal structure and stratigraphy of the South Mozambique margin to Mozambique Ridge from combined wide-angle and reflection seismic and drill hole data. Earth and Space Science. Paper #2021EA001902-TRR, in press.

Sichler, B., 1980. La biellette Danakil, un modèle pourl'évolution géodynamique des Afars. Bulletin de la Société Géologique de France 22 (6), 925–932.

Stockwell, J.W., 1999. The CWP/SU: Seismic Unx packagep. Comput. Geosci. 25, 415–419.

Talwani, M., Eldholm, O., 1977. Evolution of the Norwegian–Greenland Sea. Geol. Soc. Am. Bull. 88, 969–999. https://doi.org/10.1130/0016-7606.

Tarling, D.H., 1972. Another Gondwanaland. Nature 238, 92–93.

Thompson, J.O., Moulin, M., Aslanian, D., Guillocheau, F., de Clarens, P., 2019. New starting point for the Indian Ocean: second phase of breakup for the Gondwana. Earth Sci. Rev. 191, 26–56.

Tikku, A.A., Karen, M., Marks, K.M., Kovacs, L.C., 2002. An early cretaceous extinct spreading center in the northern Natal valley. Tectonophysics 347, 87–108.

Torsvik, T., Van der Voo, R., Preeden, U., Mac Niocaill, C., Steinberger, B., Doubrovine, P.V., van Hinsbergen, D.J.J., Domeier, M., Gaina, C., Tohver, E., Meert, J.G., McCausland, P.J.A., Cocks, L.R.M., 2012. Phanerozoic polar wander, palaeogeography and dynamics. Earth Sci. Rev. 114, 328–365.

Trompette, R., 1994. Geology of Western Gondwana 2000–500 ma: Pan-African-Brasiliano Aggregation of South America and Africa. A. A. Balkema, Rotterdam, Brookfeild, p. 350.

Watremetz, L., Leroy, S., d'Acremont, E., Roche, V., Leprêtre, A., Verrier, F., Aslanian, D., Dias, N.A., Afilhado, A., Schnürle, P., Castilla, R., Despinois, F., Moulin, M., 2021. The Limpopo magmatic transform margin (South Mozambique) – part 1: insights from deep-structure seismic imaging. Tectonics 40. https://doi.org/10.1029/2021TC006915 e2021TC006915.

Watts, A.B., 2001. Gravity anomalies, flexure and crustal structure at the Mozambique rifted margin. Mar. Petrol. Geol. 18, 445–455. https://doi.org/10.1016/S0264-8172(00)00079-9.

Wessel, P., Smith, W.H.F., 1998. New, improved version of Generic Mapping Tools released. EOS Trans. Amer. Geophys. U. 79, 579.

Zelt, C.A., 1999. Modelling strategies and model assessment for wide-angle seismic traveltime data. Geophys. J. Int. 183–204.

Zelt, C.A., Forsyth, D.A., 1994. Modeling wide-angle seismic data for crustal structure: Southeastern Grenville province. J. Geophys. Res. 99, 11687–11704. https://doi.org/10.1029/93JB02764.

Zelt, C.A., Smith, R.B., 1992. Seismic travel time inversion for 2-D crustal velocity structure. Geophys. J. Int. 108, 16–34.